Discontinuous Galerkin Methods for Relativistic Vlasov-Maxwell System

He Yang * and Fengyan Li †

December 10, 2016

Abstract

The relativistic Vlasov-Maxwell (RVM) system is a kinetic model that describes the dynamics of plasma when the charged particles move in the relativistic regime and their collisions are not important. In this paper, we formulate and investigate discontinuous Galerkin (DG) methods to solve the RVM system. When standard piecewise polynomial functions are used to define trial and test spaces, the methods conserve mass as expected. However the energy conservation does not hold due to the specific form of the total energy of the system. In order to obtain provable mass and energy conservation, we take advantage of the flexibility of DG discretizations and enrich the discrete spaces with some non-polynomial function. For the semi-discrete DG methods with standard and enriched spaces, stability and error estimates are established together with their properties in conservation. In actual implementation with the enriched space, special care is needed to reduce the loss of significance for better numerical stability. Numerical experiments, including streaming Weibel instability and wakefield acceleration, are presented to demonstrate the performance of the methods. Positivity-preserving limiter is also used in simulating wakefield acceleration to obtain physically more relevant solutions.

Keywords: relativistic Vlasov-Maxwell system, discontinuous Galerkin methods, non-polynomial space, conservation, streaming Weibel instability, wakefield acceleration

AMS(MOS) subject classification: 65M15, 65M60, 35Q83, 35L50

1 Introduction

In this paper, we formulate and investigate discontinuous Galerkin (DG) methods to solve the dimensionless relativistic Vlasov-Maxwell (RVM) equations

$$\begin{cases} \partial_t f + \dfrac{v}{\sqrt{1+|v|^2}} \cdot \nabla_x f + (E + \dfrac{v \times B}{\sqrt{1+|v|^2}}) \cdot \nabla_v f = 0, \\ \partial_t E = \nabla \times B - J, \quad \partial_t B = -\nabla \times E, \\ \nabla \cdot E = \rho - \rho_i, \quad \nabla \cdot B = 0, \end{cases} \tag{1.1}$$

and

$$\rho(x,t) = \int_{\Omega_v} f(x,v,t)dv, \quad J(x,t) = \int_{\Omega_v} \frac{fv}{\sqrt{1+|v|^2}}dv, \tag{1.2}$$

*Department of Mathematics, The Ohio State University, Columbus, OH 43210. Email: yang.1671@osu.edu

†Department of Mathematical Sciences, Rensselaer Polytechnic Institute, Troy, NY 12180. Email: lif@rpi.edu.
This research is partially supported by NSF grant DMS-1318409.

where f represents the particle number density which is the total number of particles of interest per unit volume in the phase space (x, v), ρ is the charge density, ρ_i is the charge density of the background particles, J is the current density, and E and B are electric and magnetic fields, respectively. The RVM model is widely used to describe the time evolution of collisionless charged particles in the self-consistent electromagnetic field in the relativistic regime. In non-relativistic regime, Vlasov-Maxwell (VM) equations are often considered instead.

With the broad applications of the VM/RVM systems in plasma physics, astronomy and star wind theory, many numerical methods have been developed. Particle-based methods [2, 13] are one of the most widely used methods, due to their computational efficiency especially when the phase space is of high dimensions. However, it is difficult for such methods to provide accurate approximations with the statistical noise. Instead many high order deterministic methods have been proposed to achieve better accuracy, and they include Fourier transform based methods [14, 9, 10], semi-Lagrangian methods [6, 19, 17], and classical finite element methods [23, 24]. In particular, DG methods were developed for the Vlasov-Maxwell system. In [5], semi-discrete schemes with DG discretizations in the phase space were formulated for the VM system, where stability, error estimates, and conservation properties were established when standard piecewise polynomials are used as discrete spaces. In [22], error estimates were conducted for fully-discrete schemes when the DG discretizations in phase space are coupled with a third order total variation diminishing (TVD) Runge-Kutta method in time. Fully-discrete energy-conserving DG methods were also proposed in [4]. DG methods have the advantages of being highly accurate, suitable for parallel computing and adaptive simulation, flexible with local approximations, and with excellent dispersion and dissipation behaviors. DG methods were particularly chosen in [5] and [4] for their provable property in conserving mass and energy. Our effort in this paper is to aim for similar provable properties of DG methods to solve the RVM equations. It is known that for simulation over long period of time, or on under-resolved meshes, energy-preserving methods can produce physically more relevant approximations and avoiding plasma self heating or cooling [8]. Energy preserving property also implies some nonlinear stability of the underlying methods. There has been quite much effort to develop energy conserving methods for various plasma models, with some examples including particle-in-cell solver for Vlasolv-Maxwell equations [15] and DG methods for Vlasov-Poisson equations [1].

In this work, we formulate and investigate both the standard and the enriched DG methods, with the former using standard piecewise polynomials discrete spaces, and the latter including additional non-polynomial function to enrich the discrete spaces. The enriched DG methods can be formulated quite straightforwardly due to the intrinsic flexibility of DG methods in using various local approximations. Mass conservation can be proved regardless of the discrete spaces, as the constant function $g(x, v) = 1$ is always in the test space. Provable energy conservation however depends on the choice of numerical fluxes, as discussed in [5], and the choice of discrete spaces. For the VM system, the total energy is $\int_\Omega f|v|^2 dxdv + \int_{\Omega_x}(|E|^2 + |B|^2)dx$, and it was shown in [5] that the computed total energy is conserved if the discrete space for f includes $g(x, v) = |v|^2$ and if the numerical fluxes are suitably chosen for the Maxwell solver. For the RVM system, the total energy is given as $\int_\Omega \sqrt{1+|v|^2} f dxdv + \frac{1}{2}\int_{\Omega_x}(|E|^2+|B|^2)dx$, and the presence of the non-polynomial function $\sqrt{1+|v|^2}$ in the kinetic energy challenges the standard DG methods in preserving total energy. To overcome this, we formulate DG methods with the discrete space for f enriched with this very function $\sqrt{1+|v|^2}$, motivated by the definition of the total energy.

For both the standard and enriched DG methods, stability and error estimates can be obtained by following the analysis in [5]. For the error estimates, one also needs the inverse inequalities and approximation properties for the enriched discrete spaces. Without loss of generality, these results are established in the present work when the phase space involves one dimension in x and two dimensions in v (denoted as 1D2V) and when the enriched linear discrete space $\mathcal{G}_h^{+1}$ is used. Note that all analyses are carried out for the methods in their semi-discrete forms. The accuracy

and the conservation of the methods are demonstrated through a set of numerical experiments, where a third order TVD Runge-Kutta method is applied as the temporal discretization. When the conservation properties are compared among methods, it is observed that for relatively low order methods, enriched DG methods outperform the standard DG methods. With the increase of the accuracy order, the advantage of using enriched space does not significantly improve the energy conservation. We attribute this to that the function $\sqrt{1+|v|^2}$ can be approximated more and more accurately by polynomials with their degrees increasing. For some applications such as wakefield acceleration, it is important to preserve the positivity of the particle number density f in order to capture the physics reliably. For this application, positivity-preserving technique [25] is utilized in standard DG methods, and the computed results are greatly improved. Note that with the positivity preserving technique, the methods still conserves mass yet generally will no longer preserve energy. It is a challenging task, if not impossible, to design numerical methods which can be mass and energy conserving and at the same time preserve positivity of the solution.

The rest of this paper is organized as follows. In Section 2, we define some notation and formulate DG methods. The conservation properties, stability analysis, and error estimates of the semi-discrete schemes are given in Section 3. In the same section, inverse inequalities and approximation properties are established for the enriched discrete space. In Section 4, we discuss some important aspects in actual implementations. Section 5 is devoted to the numerical demonstration of the accuracy, conservation, and robustness of the methods through examples of streaming Weibel instability and wakefield acceleration. We conclude in Section 6 with some remarks.

2 Formulations of Discontinuous Galerkin Methods

In this section, we will introduce some notation and formulate semi-discrete DG methods for the RVM system (1.1). We want to mention that the Gauss laws for E and the divergence free condition for B in (1.1) are not used in constructing our schemes. On the PDE level, these two equations can be derived from the remaining of the system, and numerically, we rely on our proposed schemes to approximate these relations.

Consider the RVM system defined on the phase domain $\Omega = \Omega_x \times \Omega_v$, with Ω_x and Ω_v being the spatial and velocity domain, respectively. Assume the velocity domain Ω_v is sufficiently large such that the particle number density function f is compactly supported in v direction. The boundary condition in x direction is assumed to be periodic. Let $T_h^\star = \{K_\star\}$ be the partition of the domain $\Omega_\star$ with $\star = x$ or v, and $K_\star$ is a simplex or (rotated) rectangular element. With this, $T_h = T_h^x \times T_h^v$ gives a partition of the computational domain Ω. In addition, let the set of the edges for $T_h^\star$ be denoted as $\mathcal{E}_\star$, and the set of the edges for T_h as $\mathcal{E} = \{T_h^x \times \mathcal{E}_v\} \cup \{\mathcal{E}_x \times T_h^v\}$. We also use $\mathcal{E}_v^b$ to represent the set of boundary edges of T_h^v, and $\mathcal{E}_v^i$ for the interior edges. In this paper, we use standard notation for the L^2- and L^∞-Sobolev space and norm. In particular, $||\cdot||_{0,D}$ denotes the L^2 norm on a bounded domain D. For the partition T_h, we define $h = \max(h_x, h_v)$ as the mesh size, where $h_\star = \max_{K_\star \in T_h^\star} \mathrm{diam}(K_\star)$ for $\star = x$ or v.

Next we introduce the discrete spaces for the approximating solutions and test functions,

$$\begin{aligned}
\mathcal{G}_h^k &= \{g : g|_K \in P^k(K), \forall K \in T_h\},\\
\mathcal{G}_h^{+k} &= \{g : g|_K = g_0 + c\sqrt{1+|v|^2},\ g_0 \in P^k(K),\ c \in \mathbb{R}, \forall K \in T_h\},\\
\mathcal{U}_h^k &= \{U : U|_{K_x} \in [P^k(K_x)]^3, \forall K_x \in T_h^x\}.
\end{aligned}$$

Here $P^k(K)$ is the set of polynomials of degree at most k on K for any nonnegative integer k. Both $\mathcal{G}_h^k$ and $\mathcal{U}_h^k$ are standard piecewise polynomial spaces often used in DG discretizations, while $\mathcal{G}_h^{+k}$ is an enriched space, with an extra non-polynomial function $\sqrt{1+|v|^2}$ in each mesh element and motivated by the objective of obtaining provable energy conserving methods. Note that each

function in the discrete spaces above is piecewise-defined. It is helpful to define its averages and jumps across each edge. Given an edge e shared by elements K_x^+ and K_x^-, with their outward unit normal vectors denoted by $n_x^\pm$, for any $g \in \mathcal{G}_h^k$ or $\mathcal{G}_h^{+k}$ with $g^\pm = g|_{K_x^\pm}$, and for any $U \in \mathcal{U}_h^k$ with $U^\pm = U|_{K_x^\pm}$, the averages of g and U across e are defined as

$$\{g\}_x = \frac{1}{2}(g^+ + g^-), \quad \{U\}_x = \frac{1}{2}(U^+ + U^-).$$

The jumps are defined as

$$[g]_x = g^+ n_x^+ + g^- n_x^-, \quad [U]_x = U^+ \cdot n_x^+ + U^- \cdot n_x^-, \quad [U]_{tan} = U^+ \times n_x^+ + U^- \times n_x^-.$$

Note that for a vector field U, $[U]_x$ defines the jump in the normal direction, while $[U]_{tan}$ defines the jump in the tangential direction. The averages and jumps for any interior edge in $\mathcal{E}_v^i$ are defined in the similar manner. For a boundary edge e in $\mathcal{E}_v^b$ with the outward unit normal vector n_v, let $[g]_v = g n_v$ and $\{g\}_v = \frac{1}{2} g$. This is consistent with the exact solution of f being compactly supported in Ω_v.

Following the well-established procedure to derive DG methods for a first order hyperbolic system, semi-discrete DG methods for the RVM system (1.1) can be formulated as follows: look for $f_h = f_h(\cdot,\cdot,t) \in \mathcal{G}_h^k$, and $E_h = E_h(\cdot,t), B_h = B_h(\cdot,t) \in \mathcal{U}_h^k$, such that

$$\begin{cases} \displaystyle\int_K \frac{\partial f_h}{\partial t} g \, dxdv = a_K(f_h, E_h, B_h; g), \quad \forall g \in \mathcal{G}_h^k \\ \displaystyle\int_{K_x} \left(\frac{\partial E_h}{\partial t} U + \frac{\partial B_h}{\partial t} V \right) dx = b_{K_x}(E_h, B_h, f_h; U, V), \quad \forall U, V \in \mathcal{U}_h^k \end{cases} \tag{2.3}$$

for any $K \in T_h$, $K_x \in T_h^x$, where

$$\begin{aligned} a_K(f_h, E_h, B_h; g) = & \int_K f_h \frac{v}{\sqrt{1+|v|^2}} \cdot \nabla_x g dxdv + \int_K f_h (E_h + \frac{v \times B_h}{\sqrt{1+|v|^2}}) \cdot \nabla_v g dxdv \qquad (2.4) \\ & - \int_{K_v} \int_{\partial K_x} \mathcal{H}_{f,x}(f_h; n_x, v) g ds_x dv - \int_{K_x} \int_{\partial K_v} \mathcal{H}_{f,v}(f_h, E_h, B_h; n_v, v) g ds_v dx, \\ b_{K_x}(B_h, E_h, f_h; U, V) = & \int_{K_x} (B_h \cdot \nabla \times U - E_h \cdot \nabla \times V) \, dx + \int_{\partial K_x} (\mathcal{H}_B(B_h; n_x) \cdot U - \mathcal{H}_E(E_h; n_x) \cdot V) \, ds_x \\ & - \int_{K_x} J_h \cdot U dx, \quad \text{and} \;\; J_h(x,t) = \int_{\Omega_v} \frac{f_h v}{\sqrt{1+|v|^2}} dv. \qquad (2.5) \end{aligned}$$

Here n_x and n_v are the outward unit normal vectors of the relevant mesh elements K_x and K_v, respectively. For the terms involving element boundary integrals in (2.4)-(2.5), the test functions g, U and V are evaluated from within the associated elements. The operators denoted by $\mathcal{H}$ with various subscripts are numerical fluxes, and they are chosen to ensure stability, accuracy, and possibly also conservation. In particular, upwind numerical fluxes are used to discretize the Vlasov equation, namely

$$\begin{aligned} \mathcal{H}_{f,x}(f_h; n_x, v) &= \frac{1}{\sqrt{1+|v|^2}} \left(\{f_h\}_x v + \frac{|v \cdot n_x| [f_h]_x}{2} \right) \cdot n_x, \\ \mathcal{H}_{f,v}(f_h, E_h, B_h; n_v, v) &= \left(\{ f_h (E_h + \frac{v \times B_h}{\sqrt{1+|v|^2}}) \}_v + \frac{1}{2} |(E_h + \frac{v \times B_h}{\sqrt{1+|v|^2}}) \cdot n_v| [f_h]_v \right) \cdot n_v. \end{aligned}$$

The dissipative nature of the upwind fluxes for the Vlasov solver is important for the stability of the proposed schemes which can in turn deal with features such as filamentation in solutions, while it does not affect the conservation of mass or energy. For the Maxwell solver, one can take

$$\mathcal{H}_B(B_h; n_x) = n_x \times \widetilde{E_h}, \quad \mathcal{H}_E(E_h; n_x) = n_x \times \widetilde{B_h}, \tag{2.6}$$

and they will be upwind with

$$\widetilde{E_h} = \left(\{E_h\}_x + \frac{1}{2}[B_h]_{tan} \right), \quad \widetilde{B_h} = \left(\{B_h\}_x - \frac{1}{2}[E_h]_{tan} \right); \tag{2.7}$$

they are central if

$$\widetilde{E_h} = \{E_h\}, \quad \widetilde{B_h} = \{B_h\}, \tag{2.8}$$

and alternating if

$$\widetilde{E_h} = E_h^+, \widetilde{B_h} = B_h^- \text{ or } \quad \widetilde{E_h} = E_h^-, \widetilde{B_h} = B_h^+. \tag{2.9}$$

It will be seen later that the central or alternating flux is important for achieving the conservation of the total energy, defined as

$$\int_\Omega \sqrt{1+|v|^2} f dx dv + \frac{1}{2}\int_{\Omega_x} (|E|^2 + |B|^2) dx. \tag{2.10}$$

Note that the kinetic energy includes a non-polynomial $\sqrt{1+|v|^2}$ as a factor. The standard DG methods, that use piecewise polynomial space $\mathcal{G}_h^k$ hence exclude the test function $g = \sqrt{1+|v|^2}$, can not satisfy the energy conservation theoretically. In order to have provable energy conservation, our second type of the proposed semi-discrete DG method is formulated by simply replacing the trial and test space $\mathcal{G}_h^k$ by the enriched discrete space $\mathcal{G}_h^{+k}$, while keeping all the other ingredients of the standard DG schemes unchanged. The resulted methods will be termed as the enriched DG methods. For both the standard and enriched DG methods, the numerical solutions at $t = 0$ are initialized by taking the L^2 projection of the given initial data onto either $\mathcal{G}_h^k$ or $\mathcal{G}_h^{+k}$ for f, and onto $\mathcal{U}_h^k$ for E and B.

We further introduce

$$a_h(f_h, E_h, B_h; g) = \sum_{K \in T_h} a_K(f_h, E_h, B_h; g), \quad b_h(E_h, B_h, f_h; U, V) = \sum_{K_x \in T_h^x} b_{K_x}(E_h, B_h, f_h; U, V),$$

and the following can be verified directly

$$\begin{aligned} & a_h(f_h, E_h, B_h; g) \\ = & \int_\Omega f_h v \cdot \nabla_x g dx dv + \int_\Omega f_h (E_h + \frac{v}{\sqrt{1+|v|^2}} \times B_h) \cdot \nabla_v g dx dv \\ - & \int_{T_h^v} \int_{\mathcal{E}_x} \left(\{f_h v\}_x + \frac{|v \cdot n_x|}{2} [f_h]_x \right) \cdot [g]_x ds_x dv \\ - & \int_{T_h^x} \int_{\mathcal{E}_v} \left(\{f_h (E_h + \frac{v}{\sqrt{1+|v|^2}} \times B_h)\}_v + \frac{1}{2} |(E_h + \frac{v}{\sqrt{1+|v|^2}} \times B_h) \cdot n_v| [f_h]_v \right) \cdot [g]_v ds_v dx \end{aligned} \tag{2.11}$$

and

$$\begin{aligned} & b_h(E_h, B_h, f_h; U, V) \\ = & \int_{\Omega_x} (B_h \cdot \nabla \times U - E_h \cdot \nabla \times V) \, dx + \int_{\mathcal{E}_x} \left(\widetilde{B_h} \cdot [U]_{tan} - \widetilde{E_h} \cdot [V]_{tan} \right) ds_x - \int_{\Omega_x} J_h \cdot U dx. \end{aligned} \tag{2.12}$$

3 Conservation, Stability and Error Estimates

In this section, we will examine theoretically the conservation properties, stability, and error estimates of the standard and enriched DG methods proposed in Section 2 in their semi-discrete forms. In particular, Section 3.1 is devoted to the mass conservation and stability of both methods, while the energy conservation is obtained only for the enriched DG methods. Error estimates will be established in Section 3.2, and they are closely related to that in [5] for standard DG methods solving the VM system. Our presentation will particularly focus on the new aspects associated with the use of the enriched spaces, namely their inverse inequalities and approximation properties. One can refer to [5] for more details of the error analysis proof.

3.1 Conservation and stability

Theorem 3.1. (Mass Conservation) *For both the standard and enriched DG methods, the numerical solution* (f_h, E_h, B_h) *satisfies*

$$\frac{d}{dt}\int_{\mathcal{T}_h} f_h dxdv = -\int_{\mathcal{T}_h^x}\int_{\mathcal{E}_v^b} f_h \max((E_h + \frac{v}{\sqrt{1+|v|^2}} \times B_h)\cdot n_v, 0) ds_v dx. \tag{3.13}$$

The theorem above can be obtained by taking the test function $g = 1$ in (2.3), using the explicit form of a_h in (2.11), as well as the periodic boundary condition in x and compactly supported boundary condition in v. The detail is omitted. The term on the right hand side of (3.13) measures the effect of the choice of the computational domain in velocity v. It will be on the machine accuracy level as long as the velocity domain is taken to be large enough.

The enriched DG methods can further conserve the total energy, provided that either the central or alternating flux is used in the Maxwell solver. If the upwind flux is used instead, the total energy will dissipate. We want to emphasize that the use of the upwind flux in the Vlasov solver will not affect the conservation properties of the schemes. The next lemma collects the major steps to prove the energy conservation.

Lemma 3.2. *For the enriched DG methods, the following equalities hold for the numerical solution* (f_h, E_h, B_h).
(i)

$$\begin{aligned} & a_h(f_h, E_h, B_h; \sqrt{1+|v|^2}) \\ = & \int_{\Omega_x} J_h \cdot E_h dxdv - \int_{\Omega_x}\int_{\mathcal{E}_v^b} f_h \sqrt{1+|v|^2} \max\left((E_h + \frac{v}{\sqrt{1+|v|^2}} \times B_h)\cdot n_v, 0\right) ds_v dx. \end{aligned} \tag{3.14}$$

(ii) If the central or alternating flux is used in the Maxwell solver, then

$$b_h(E_h, B_h, f_h; E_h, B_h) = -\int_{\Omega_x} J_h \cdot E_h dx. \tag{3.15}$$

(iii) If the upwind numerical flux is used in the Maxwell solver, then

$$b_h(E_h, B_h, f_h; E_h, B_h) = -\int_{\Omega_x} J_h \cdot E_h dx - \frac{1}{2}\int_{\mathcal{E}_x} \left(|[E_h]_{tan}|^2 + |[B_h]_{tan}|^2\right) ds_x. \tag{3.16}$$

Proof. For part (i), we take $g = \sqrt{1+|v|^2} \in \mathcal{G}_h^{+k}$ in the scheme (2.3), sum up with respect to $K \in T_h$, and use the compact formulation for a_h in (2.11). One can easily see that $\nabla_x \sqrt{1+|v|^2} = 0$,

$\nabla_v \sqrt{1+|v|^2} = \frac{v}{\sqrt{1+|v|^2}}$, $[\sqrt{1+|v|^2}]_x = 0$ on $\mathcal{E}_x$, $[\sqrt{1+|v|^2}]_v = 0$ on $\mathcal{E}_v^i$, and $[\sqrt{1+|v|^2}]_v = \sqrt{1+|v|^2} n_v$ on $\mathcal{E}_v^b$. These will lead to (3.14).

For part (ii), we take $U = E_h$ and $V = B_h$ in the scheme (2.3), sum up with respect to $K_x \in T_h^x$, and use the compact formulation for b_h in (2.12). We further make use of the following equalities:

$$\int_{\Omega_x} (B_h \cdot \nabla \times E_h - E_h \cdot \nabla \times B_h)\, dx = \int_{\mathcal{E}_x} [E_h \times B_h]_x ds_x, \tag{3.17}$$

$$[E_h \times B_h]_x + \{B_h\}_x \cdot [E_h]_{tan} - \{E_h\}_x \cdot [B_h]_{tan} = 0, \tag{3.18}$$

and the specific definition of the central and alternating numerical fluxes in (2.8) and (2.9) for the Maxwell solver, and this will lead to (ii). Part (iii) can be shown similarly using the definition of the upwind flux (2.7) for the Maxwell solver. □

For the proposed enriched DG methods, if we take $g = \sqrt{1+|v|^2}$, $U = E_h$ and $V = B_h$ in (2.3) and sum over all mesh elements, we will obtain

$$\begin{aligned} & \frac{d}{dt}\left(\int_{\mathcal{T}_h} \sqrt{1+|v|^2} f_h dx dv + \frac{1}{2} \int_{\mathcal{T}_h^x} (|E_h|^2 + |B_h|^2) dx \right) \\ = \;& a_h(f_h, E_h, B_h; \sqrt{1+|v|^2}) + b_h(E_h, B_h, f_h; E_h, B_h). \end{aligned} \tag{3.19}$$

Combining Lemma 3.2 and the equality (3.19), one will get the results on energy conservation.

Theorem 3.3. (Energy Conservation) *For the enriched DG methods, the numerical solution (f_h, E_h, B_h) satisfies*

$$\begin{aligned} & \frac{d}{dt}\left(\int_{\mathcal{T}_h} \sqrt{1+|v|^2} f_h dx dv + \frac{1}{2} \int_{\mathcal{T}_h^x} (|E_h|^2 + |B_h|^2) dx \right) \\ = \;& \begin{cases} I_1 & \text{with the central (2.8) or alternating (2.9) flux} \\ I_1 + I_2 & \text{with the upwind (2.7) flux} \end{cases} \end{aligned} \tag{3.20}$$

where

$$I_1 = -\int_{\mathcal{T}_h^x} \int_{\mathcal{E}_v^b} f_h \sqrt{1+|v|^2} \max((E_h + \frac{v}{\sqrt{1+|v|^2}} \times B_h) \cdot n_v, 0) ds_v dx \tag{3.21}$$

$$I_2 = -\frac{1}{2} \int_{\mathcal{E}_x} \left(|[E_h]_{tan}|^2 + |[B_h]_{tan}|^2 \right) ds_x. \tag{3.22}$$

In Theorem 3.3, the enriched discrete space $\mathcal{G}_h^{+k}$ is crucial in achieving the provable energy equalities (3.20), and it ensures that the test function g can be taken as a non-polynomial function $\sqrt{1+|v|^2}$. Moreover, the term I_1 measures the boundary effect, which is at the machine accuracy level as long as the domain in v is chosen to be large enough. The I_2 term comes from the dissipative nature of the upwind flux in the Maxwell solver. Finally, by following a similar proof of Lemma 3.7 in [5] by taking g in (2.3) to be f_h, one can establish the stability result for f in all the proposed schemes.

Theorem 3.4. (Stability in f) *For both the standard and enriched DG methods, the numerical solution (f_h, E_h, B_h) satisfies*

$$\begin{aligned} \frac{d}{dt} \int_{\mathcal{T}_h} |f_h|^2 dx dv \;+\; & \int_{\mathcal{T}_h^v} \int_{\mathcal{E}_x} \left| \frac{v}{\sqrt{1+|v|^2}} \cdot n_x \right| |[f_h]_x|^2 \, ds_x dv \\ + \; & \int_{\mathcal{T}_h^x} \int_{\mathcal{E}_x} \left| \left(E_h + \frac{v}{\sqrt{1+|v|^2}} \times B_h \right) \cdot n_v \right| |[f_h]_v|^2 \, ds_v dx = 0. \end{aligned} \tag{3.23}$$

3.2 Error estimates

In order to obtain the error estimates, three additional assumptions are made.

1. Both $\Omega_x \subset \mathbb{R}^{d_x}$ and $\Omega_v \subset \mathbb{R}^{d_v}$ are tensor-type bounded domains.
2. When the mesh is refined, both $\frac{h_x}{h_{v,\min}} := \frac{h_x}{\min_{K_v \in T_h^v} h_{K_v}}$ and $\frac{h_v}{h_{x,\min}} := \frac{h_v}{\min_{K_x \in T_h^x} h_{K_x}}$ are uniformly bounded above by a positive constant σ_0.
3. The exact solution (f, E, B) of the RVM system has sufficient regularity.

We use C to represent a generic constant, and its value can be different at different occurances.

Theorem 3.5. (Error Estimates) *Let $(f_h, E_h, B_h) \in \mathcal{G}_h^k \times \mathcal{U}_h^k \times \mathcal{U}_h^k$ be the solution to the standard DG method (2.3) with $k \geq \frac{d_x+1}{2}$, then*

$$||f(\cdot,\cdot,t) - f_h(\cdot,\cdot,t)||_{0,\Omega}^2 + ||E(\cdot,t) - E_h(\cdot,t)||_{0,\Omega_x}^2 + ||B(\cdot,t) - B_h(\cdot,t)||_{0,\Omega_x}^2 \leq Ch^{2k+1} \tag{3.24}$$

if the upwind flux is used in the Maxwell solver; and

$$||f(\cdot,\cdot,t) - f_h(\cdot,\cdot,t)||_{0,\Omega}^2 + ||E(\cdot,t) - E_h(\cdot,t)||_{0,\Omega_x}^2 + ||B(\cdot,t) - B_h(\cdot,t)||_{0,\Omega_x}^2 \leq Ch^{2k} \tag{3.25}$$

if the central or alternating flux is used in the Maxwell solver. In addition, if the mesh T_h is Cartesian, the estimates (3.24)-(3.25) above also hold for the numerical solution $(f_h, E_h, B_h) \in \mathcal{G}_h^{+k} \times \mathcal{U}_h^k \times \mathcal{U}_h^k$ of the enriched DG methods. Here the generic constant C depends on the exact solution (in their Sobolev norms) up to time t, mesh parameter σ_0, polynomial degree k, and the domain Ω, yet it is independent of the mesh size h.

For the standard DG methods , the error estimates (3.24)-(3.25) can be obtained essentially in the same way as that of Theorems 4.3 and 4.6 in [5], where standard DG methods for VM equations are analyzed. The restriction for k, namely $k \geq \frac{d_x+1}{2}$, is due to the lack of the L^∞ error estimates for the DG solutions of the Maxwell part. In order to establish the error estimates for the enriched DG methods, analysis similar to [5] can be carried out, as long as some inverse inequalities and approximation properties hold for the enriched discrete space $\mathcal{G}_h^{+k}$. To better present the technical aspects without loss of generality, these results will be established only for $\mathcal{G}_h^{+k}$ with $k = 1$ and when the phase space involves one dimension in x and two dimensions in v (denoted as 1D2V), see Lemma 3.7 - Lemma 3.9. The mesh is assumed to be Cartesian, so is the one in Theorem 3.5. All the results for the enriched DG methods can be extended to higher k and other phase space dimensions, as well as to general meshes, with more involved analysis. With the restriction $k \geq \frac{d_x+1}{2}$, our error analysis is not applicable to the case $k = 0$ for any spatial dimension.

Let $K = [\bar{x}_2 - \frac{1}{2}h_{x_2}, \bar{x}_2 + \frac{1}{2}h_{x_2}] \times [\bar{v}_1 - \frac{1}{2}h_{v_1}, \bar{v}_1 + \frac{1}{2}h_{v_1}] \times [\bar{v}_2 - \frac{1}{2}h_{v_2}, \bar{v}_2 + \frac{1}{2}h_{v_2}]$, where $(\bar{x}_2, \bar{v}_1, \bar{v}_2)$ is the center of the element K, and let $\mathcal{P}_h^{+1} = \mathcal{P}_h^{+1}(K) = \text{span}\{1, x_2, v_1, v_2, \sqrt{1 + v_1^2 + v_2^2}\}$. For this local space $\mathcal{P}_h^{+1}$, one set of basis is given as follows,

$$\varphi_1 = 1, \;\; \varphi_2 = \frac{x_2 - \bar{x}_2}{h_{x_2}}, \;\; \varphi_3 = \frac{v_1 - \bar{v}_1}{h_{v_1}}, \;\; \varphi_4 = \frac{v_2 - \bar{v}_2}{h_{v_2}}, \;\; \varphi_5 = \sqrt{1 + v_1^2 + v_2^2}. \tag{3.26}$$

From this, one can get another set of basis $\{\phi_m\}_{m=1}^5$ that is orthogonal over K, satisfying

$$\phi_n = \varphi_n, n = 1, 2, 3, 4, \;\; \phi_5 = \sum_{n=1}^{5} a_n \varphi_n, \text{ such that } (\phi_n, \phi_m) = \delta_{nm} \text{ and } ||\phi_5||_{0,K} = \sqrt{h_{x_2} h_{v_1} h_{v_2}}. \tag{3.27}$$

Here and below in this section, $(\cdot,\cdot)$ represents the L^2 inner product over K. In addition, when the big-O, $O(1)$, is used, the hidden constant depends only on the size of Ω_v, yet not on h_{x_2}, h_{v_1} and h_{v_2} hence not on h. We next summarize some results about the orthogonal basis before turning to building inverse inequalities and approximation results for $\mathcal{P}_h^{+1}$.

Lemma 3.6. (Properties of the Basis $\{\phi_m\}_{m=1}^5$) *The following hold for the orthogonal basis $\{\phi_m\}_{m=1}^5$ in (3.27):*

$$a_n = -\tfrac{(\varphi_n,\varphi_5)}{(\varphi_n,\varphi_n)}a_5, \quad n=1,\dots,4, \tag{3.28}$$

$$\tfrac{(\varphi_n,\varphi_5)}{(\varphi_n,\varphi_n)} = O(1), \quad n=1,\dots,4, \tag{3.29}$$

$$a_n = O(1), \quad n=1,\dots,5. \tag{3.30}$$

In fact, $a_2 = 0$.

Proof. It is easy to see the relation (3.28) and $a_2 = 0$ from (3.27). To get the results in (3.29), note that

$$(\varphi_3,\varphi_5) = \left(\frac{v_1-\bar{v}_1}{h_{v_1}}, \sqrt{1+v_1^2+v_2^2}\right) = O(h_{x_2}h_{v_1}h_{v_2}), \quad (\varphi_3,\varphi_3) = \frac{1}{12}h_{x_2}h_{v_1}h_{v_2}, \tag{3.31}$$

and this implies (3.29) with $n=3$. Similarly (3.29) holds for other n. For the results in (3.30), we only need to estimate a_5, and the other will follow. Based on (3.27)-(3.29), we know

$$\begin{aligned} h_{x_2}h_{v_1}h_{v_2} &= ||\phi_5||_{0,K}^2 = a_5^2||\varphi_5 - \frac{(\varphi_5,\varphi_1)}{(\varphi_1,\varphi_1)}\varphi_1 - \frac{(\varphi_5,\varphi_3)}{(\varphi_3,\varphi_3)}\varphi_3 - \frac{(\varphi_5,\varphi_4)}{(\varphi_4,\varphi_4)}\varphi_4||_{0,K}^2 \\ &= a_5^2||\varphi_5 - O(1)\varphi_1 - O(1)\varphi_3 - O(1)\varphi_4||_{0,K}^2 = a_5^2\cdot O(h_{x_2}h_{v_1}h_{v_2}), \end{aligned} \tag{3.32}$$

and this will give $a_5 = O(1)$.

□

Lemma 3.7. (Inverse Inequality) *There exists a constant $C>0$, such that for any $g\in\mathcal{P}_h^{+1}$, we have*

$$||\frac{\partial g}{\partial v_1}||_{0,K} \le Ch_{v_1}^{-1}||g||_{0,K}, \quad ||\frac{\partial g}{\partial v_2}||_{0,K} \le Ch_{v_2}^{-1}||g||_{0,K}, \quad ||\frac{\partial g}{\partial x_2}||_{0,K} \le Ch_{x_2}^{-1}||g||_{0,K}. \tag{3.33}$$

Here the constant C is independent of h_{x_2}, h_{v_1} and h_{v_2}, and depends on the size of Ω_v.

Proof. Consider $\forall g = \sum_{m=1}^5 c_m\phi_m \in \mathcal{P}_h^{+1}$, then

$$||\frac{\partial g}{\partial v_1}||_{0,K}^2 = ||\sum_{m=1}^5 c_m\frac{\partial\phi_m}{\partial v_1}||_{0,K}^2 = ||c_3\frac{\partial\phi_3}{\partial v_1} + c_5\frac{\partial\phi_5}{\partial v_1}||_{0,K}^2 = \mathbf{c}^TA\mathbf{c}, \tag{3.34}$$

where

$$A = \begin{pmatrix} 0 & & & & \\ & 0 & & & \\ & & ||\frac{\partial\phi_3}{\partial v_1}||_{0,K}^2 & & \left(\frac{\partial\phi_3}{\partial v_1},\frac{\partial\phi_5}{\partial v_1}\right) \\ & & & 0 & \\ & & \left(\frac{\partial\phi_5}{\partial v_1},\frac{\partial\phi_3}{\partial v_1}\right) & & ||\frac{\partial\phi_5}{\partial v_1}||_{0,K}^2 \end{pmatrix}$$

and $\mathbf{c} = (c_1,c_2,c_3,c_4,c_5)^T$. Similarly, we can write

$$||g||_{0,K}^2 = \mathbf{c}^TM\mathbf{c}, \tag{3.35}$$

with $M = h_{x_2}h_{v_1}h_{v_2}\text{diag}(1, 1/12, 1/12, 1/12, 1)$. Note that both A and M are symmetric. In addition, M is positive definite and A is positive semi-definite. In order to find a constant C such that $||\frac{\partial g}{\partial v_1}||_{0,K} \leq C||g||_{0,K},\ \forall g \in \mathcal{P}_h^{+1}$, it is equivalent to finding the upper bound C of the eigenvalues of the following generalized eigenvalue problem

$$A\mathbf{c} = \lambda M\mathbf{c} \Leftrightarrow M^{-1}A\mathbf{c} = \lambda\mathbf{c}, \quad \mathbf{c} \neq \mathbf{0}.$$

Here

$$M^{-1}A = \frac{1}{h_{x_2}h_{v_1}h_{v_2}} \begin{pmatrix} 0 & & & & \\ & 0 & & & \\ & & 12||\frac{\partial\phi_3}{\partial v_1}||_{0,K}^2 & & 12\left(\frac{\partial\phi_3}{\partial v_1}, \frac{\partial\phi_5}{\partial v_1}\right) \\ & & & 0 & \\ & & \left(\frac{\partial\phi_5}{\partial v_1}, \frac{\partial\phi_3}{\partial v_1}\right) & & ||\frac{\partial\phi_5}{\partial v_1}||_{0,K}^2 \end{pmatrix}$$

and it has two nonzero eigenvalues

$$\lambda_{1,2} = \frac{12\alpha^2 + \beta^2 \pm \sqrt{(12\alpha^2 - \beta^2)^2 + 48\gamma^2}}{2h_{x_2}h_{v_1}h_{v_2}}, \tag{3.36}$$

where $\alpha = ||\frac{\partial\phi_3}{\partial v_1}||_{0,K}$, $\beta = ||\frac{\partial\phi_5}{\partial v_1}||_{0,K}$ and $\gamma = (\frac{\partial\phi_5}{\partial v_1}, \frac{\partial\phi_3}{\partial v_1})$. There two eigenvalues can be bounded above as follows,

$$|\lambda_{1,2}| \leq \frac{12\alpha^2 + \beta^2 + 2\sqrt{3}|\gamma|}{h_{x_2}h_{v_1}h_{v_2}} \leq \frac{12\alpha^2 + \beta^2 + 2\sqrt{3}\alpha\beta}{h_{x_2}h_{v_1}h_{v_2}} \leq \frac{(12 + \sqrt{3})\alpha^2 + (1 + \sqrt{3})\beta^2}{h_{x_2}h_{v_1}h_{v_2}}. \tag{3.37}$$

With a direct calculation as well as the fact $a_3 = O(1), a_5 = O(1)$ in (3.30), one gets

$$\alpha^2 = \frac{h_{x_2}h_{v_1}h_{v_2}}{h_{v_1}^2}, \tag{3.38}$$

$$\beta^2 = ||\frac{\partial\phi_5}{\partial v_1}||_{0,K}^2 = ||\frac{a_3}{h_{v_1}} - \frac{a_5 v_1}{\sqrt{1 + v_1^2 + v_2^2}}||_{0,K}^2 = O(\frac{1}{h_{v_1}^2})(h_{x_2}h_{v_1}h_{v_2}). \tag{3.39}$$

Now we can assemble the estimates in (3.37)-(3.39), and get $|\lambda_{1,2}| = O(\frac{1}{h_{v_1}^2})$. This implies the first estimate in (3.33). The other estimates can be shown similarly. □

Let Π^1 and Π^{+1} be the L^2 projections onto $\mathcal{P}_h^1 = P^1(K)$ and $\mathcal{P}_h^{+1}$, respectively. The following approximation results hold.

Lemma 3.8. (Approximation Property of Π^{+1}: I) *There exists a constant $C > 0$, such that $\forall g \in H^2(K)$, we have*

$$||g - \Pi^{+1}g||_{0,K} + h|g - \Pi^{+1}g|_{1,K} + h^{1/2}||g - \Pi^{+1}g||_{0,\partial K} \leq Ch^2||g||_{2,K}. \tag{3.40}$$

Here the constant C is independent of h and depends on the size of Ω_v and the mesh parameter σ_0.

Proof. Given $\mathcal{P}_h^1 \subset \mathcal{P}_h^{+1}$, we get

$$||g - \Pi^{+1}g||_{0,K} \leq ||g - \Pi^1 g||_{0,K}. \tag{3.41}$$

For $|g - \Pi^{+1}g|_{1,K}$, we apply triangle inequality, Lemma 3.7, and obtain

$$\begin{aligned} |g - \Pi^{+1}g|_{1,K} &\leq |g - \Pi^1 g|_{1,K} + |\Pi^1 g - \Pi^{+1}g|_{1,K} \\ &\leq |g - \Pi^1 g|_{1,K} + \frac{C}{h}||\Pi^1 g - \Pi^{+1}g||_{0,K}, \end{aligned}$$

where

$$||\Pi^1 g - \Pi^{+1} g||_{0,K} = ||\Pi^{+1}(g - \Pi^1 g)||_{0,K} \leq ||g - \Pi^1 g||_{0,K},$$

therefore

$$|g - \Pi^{+1} g|_{1,K} \leq |g - \Pi^1 g|_{1,K} + \frac{C}{h}||g - \Pi^1 g||_{0,K}. \tag{3.42}$$

Now we can conclude (3.40) by combining (3.41) and (3.42) with the approximation results for the standard piecewise polynomial space [7, 5], namely

$$||g - \Pi^1 g||_{0,K} + h|g - \Pi^1 g|_{1,K} \leq Ch^2||g||_{2,K}, \quad \forall g \in H^2(K) \tag{3.43}$$

as well as the trace inequality: $||u||^2_{0,\partial K} \leq C||u||_{0,K}|u|_{1,K}$, $\forall u \in H^1(K)$. Here the constant C is independent of h_{x_2}, h_{v_1} and h_{v_2}, and depends on the mesh parameter σ_0 and the size of Ω_v. □

Lemma 3.9. (Approximation Property of Π^{+1}: II) *There exists a constant $C > 0$, such that $\forall f \in H^2(K)$ and $\forall g \in \mathcal{P}_h^{+1}$, the following estimates hold*

$$\left| \int_K \left(f - \Pi^{+1} f\right) \frac{\partial g}{\partial v_1} dxdv \right| \leq C||g||_{0,K}||f||_{2,K}h^4, \tag{3.44}$$

$$\left| \int_K \left(f - \Pi^{+1} f\right) \frac{\partial g}{\partial v_2} dxdv \right| \leq C||g||_{0,K}||f||_{2,K}h^4. \tag{3.45}$$

Here the constant C is independent of h, and depends on the size of Ω_v and the mesh parameter σ_0.

Proof. With similarity, we will only prove (3.44). Consider $\forall g = \sum_{m=1}^5 c_m\phi_m \in \mathcal{P}_h^{+1}$. Based on the orthogonality of $\{\phi_m\}_{m=1}^5$ and the property of ϕ_5 in (3.27), we know $||g||_{0,K} \geq |c_5|||\phi_5||_{0,K} = |c_5|\sqrt{h_{x_2}h_{v_1}h_{v_2}}$. That is

$$|c_5| \leq \frac{||g||_{0,K}}{\sqrt{h_{x_2}h_{v_1}h_{v_2}}}. \tag{3.46}$$

Since $\frac{\partial \phi_m}{\partial v_1} \in \mathcal{P}_h^{+1}$ for $m = 1, \ldots, 4$, we have

$$\begin{aligned}
\left| \int_K \left(f - \Pi^{+1} f\right) \frac{\partial g}{\partial v_1} dxdv \right| &= \left| c_5 \int_K \left(f - \Pi^{+1} f\right) \frac{\partial \phi_5}{\partial v_1} dxdv \right| \\
&= \left| c_5 \int_K \left(f - \Pi^{+1} f\right) \left(\Pi^{+1} \frac{\partial \phi_5}{\partial v_1} - \frac{\partial \phi_5}{\partial v_1}\right) dxdv \right| \\
&\leq |c_5|||f - \Pi^{+1} f||_{0,K} \left\| \Pi^{+1} \frac{\partial \phi_5}{\partial v_1} - \frac{\partial \phi_5}{\partial v_1} \right\|_{0,K} \\
&\leq \frac{Ch^2}{\sqrt{h_{x_2}h_{v_1}h_{v_2}}} ||g||_{0,K}||f||_{2,K} \left\| \Pi^{+1} \frac{\partial \phi_5}{\partial v_1} - \frac{\partial \phi_5}{\partial v_1} \right\|_{0,K}.
\end{aligned} \tag{3.47}$$

In the last inequality, we have used Lemma 3.8 and the estimate (3.46).

What remained is to estimate the term $\left\| \Pi^{+1} \frac{\partial \phi_5}{\partial v_1} - \frac{\partial \phi_5}{\partial v_1} \right\|_{0,K}$. It can be seen easily that $\frac{\partial \phi_5}{\partial v_1} = \frac{a_3}{h_{v_1}} + a_5 \frac{v_1}{\sqrt{1+v_1^2+v_2^2}}$ and $\Pi^{+1} \frac{\partial \phi_5}{\partial v_1} = \frac{a_3}{h_{v_1}} + a_5 \Pi^{+1} \frac{v_1}{\sqrt{1+v_1^2+v_2^2}}$. By applying Lemma 3.8 and the fact $a_5 = O(1)$ in (3.30), we reach

$$\left\| \Pi^{+1} \frac{\partial \phi_5}{\partial v_1} - \frac{\partial \phi_5}{\partial v_1} \right\|_{0,K} \leq Ch^2 \left\| \frac{v_1}{\sqrt{1 + v_1^2 + v_2^2}} \right\|_{2,K} \leq C\sqrt{h_{x_2}h_{v_1}h_{v_2}}h^2. \tag{3.48}$$

The last inequality is due to that $\frac{v_1}{\sqrt{1+v_1^2+v_2^2}} \in W^{2,\infty}(\Omega_v)$. And the two constants C in (3.48) take different values. We can now conclude (3.44) by combining (3.47) and (3.48). □

Lemma 3.10. (Approximation Property of Π^{+1}: III) *There exists a constant $C > 0$, such that $\forall f \in H^2(K)$ and $\forall g \in \mathcal{P}_h^{+1}$, the following estimates hold*

$$\left| \int_K \left(f - \Pi^{+1} f\right) \frac{v_2}{\sqrt{1+v_1^2+v_2^2}} \frac{\partial g}{\partial v_1} dxdv \right| \leq C||g||_{0,K}||f||_{2,K}h^3, \tag{3.49}$$

$$\left| \int_K \left(f - \Pi^{+1} f\right) \frac{v_1}{\sqrt{1+v_1^2+v_2^2}} \frac{\partial g}{\partial v_2} dxdv \right| \leq C||g||_{0,K}||f||_{2,K}h^3. \tag{3.50}$$

Here the constant C is independent of h, and depends on the size of Ω_v and the mesh parameter σ_0.

Proof. With similarity, we will only prove (3.49). For $\forall g = \sum_{m=1}^5 c_m \phi_m \in \mathcal{P}_h^{+1}$, recall the definition of $\{\phi_m\}_{m=1}^5$ in (3.27), one can derive the following

$$\frac{v_2}{\sqrt{1+v_1^2+v_2^2}} \frac{\partial g}{\partial v_1} = \frac{v_2}{\sqrt{1+v_1^2+v_2^2}} \left((c_3 + c_5 a_3) \frac{1}{h_{v_1}} + c_5 a_5 \frac{v_1}{\sqrt{1+v_1^2+v_2^2}} \right). \tag{3.51}$$

Therefore we have

$$\begin{aligned}
& \left| \int_K \left(f - \Pi^{+1} f\right) \frac{v_2}{\sqrt{1+v_1^2+v_2^2}} \frac{\partial g}{\partial v_1} dxdv \right| \\
\leq & \left| \frac{c_3 + c_5 a_3}{h_{v_1}} \int_K \left(f - \Pi^{+1} f\right) \frac{v_2}{\sqrt{1+v_1^2+v_2^2}} dxdv \right| + \left| c_5 a_5 \int_K \left(f - \Pi^{+1} f\right) \frac{v_1 v_2}{1+v_1^2+v_2^2} dxdv \right| \\
\leq & \left| \frac{c_3 + c_5 a_3}{h_{v_1}} \right| \|f - \Pi^{+1} f\|_{0,K} \left\| \frac{v_2}{\sqrt{1+v_1^2+v_2^2}} - \Pi^{+1} \frac{v_2}{\sqrt{1+v_1^2+v_2^2}} \right\|_{0,K} \\
& + |c_5 a_5| \|f - \Pi^{+1} f\|_{0,K} \left\| \frac{v_1 v_2}{1+v_1^2+v_2^2} - \Pi^{+1} \frac{v_1 v_2}{1+v_1^2+v_2^2} \right\|_{0,K} \\
\leq & Ch^4 \|f\|_{2,K} \frac{|c_3| + |c_5 a_3|}{h_{v_1}} \left\| \frac{v_2}{\sqrt{1+v_1^2+v_2^2}} \right\|_{2,K} + Ch^4 \|f\|_{2,K} |c_5 a_5| \left\| \frac{v_1 v_2}{1+v_1^2+v_2^2} \right\|_{2,K} \\
\leq & C\sqrt{h_{x_2} h_{v_1} h_{v_2}} h^4 \|f\|_{2,K} \left(\frac{|c_3| + |c_5|}{h_{v_1}} \right).
\end{aligned} \tag{3.52}$$

We have used Lemma 3.8, the fact that $\frac{v_2}{\sqrt{1+v_1^2+v_2^2}}, \frac{v_1 v_2}{1+v_1^2+v_2^2} \in W^{2,\infty}(\Omega_v)$, as well as the boundedness of a_3 and a_5 in (3.30).

The final step of the proof is to bound $|c_3|$ and $|c_5|$. Due to the orthogonality of $\{\phi_m\}_{m=1}^5$, one gets $\|g\|_{0,K}^2 \geq ||c_3\phi_3||_{0,K}^2 + ||c_5\phi_5||_{0,K}^2 = (\frac{1}{12}c_3^2 + c_5^2) h_{x_2} h_{v_1} h_{v_2}$, and therefore

$$|c_3|, |c_5| \leq \frac{2\sqrt{3}\|g\|_{0,K}}{\sqrt{h_{x_2} h_{v_1} h_{v_2}}}.$$

We can now obtain the estimate (3.49) by combining (3.52) with the bounds for $|c_m|$, $m = 3, 5$. □

4 On Implementation

In our implementation, a third order total variation diminishing Runge-Kutta (TVD-RK) method [18] is applied to solve the ODE system resulted from the semi-discrete DG methods (2.3) for the RVM system. That is, given an ODE system $\frac{d}{dt}R = L(R,t)$, and its approximation R^n at time t_n, then $R^{n+1} \approx R(t_{n+1})$ is computed as follows:

$$\begin{aligned} R^{n,1} &= R^n + \Delta t L(R^n, t_n), \\ R^{n,2} &= \frac{3}{4}R^n + \frac{1}{4}R^{n,1} + \frac{1}{4}\Delta t L(R^{n,1}, t_{n+1}), \\ R^{n+1} &= \frac{1}{3}R^n + \frac{2}{3}R^{n,2} + \frac{2}{3}\Delta t L(R^{n,2}, t_n + \frac{1}{2}\Delta t). \end{aligned}$$

Here $\Delta t = t_{n+1} - t_n$.

Even though the enriched DG methods have provable energy conservation property (see Theorem 3.3), extra care is needed for numerical stability when such methods are implemented. This is due to the inclusion of the non-polynomial function $\sqrt{1+|v|^2}$ in the local space and its accompanied ill-conditioning. In our numerical experiments in Section 5, enriched DG methods with $\mathcal{G}_h^{+k}, k = 0, 1, 2$ are implemented. The added function $\sqrt{1+|v|^2}$ can be nearly linearly dependent of other local basis functions such as 1 or some component of v variable in some region. For example, $\sqrt{1+|v|^2}$ and 1 are nearly linear independent where $|v|$ is close to 0. Ill-conditioning issue related to using non-standard discrete spaces in DG methods were addressed in literatures, for instance for plane-wave DG methods [12, 11].

To avoid the poor conditioning of the mass matrix for the enriched discrete space, we use locally orthogonal basis for $\mathcal{G}_h^{+k}$. For instance, for $\mathcal{G}_h^{+1}|_K, K \in T_h$, the basis set just like $\{\phi_m\}_{m=1}^5$ in (3.27) is used locally. (We omit the K-dependence of the notation ϕ_m.) With this choice, the local mass matrix is diagonal and independent of $K \in T_h$. Now the mass matrix is well-conditioned, yet the original ill-conditioning is converted to the ill-conditioning to compute the expansion coefficients, such as $\{a_m\}_{m=1}^5$ in (3.27), from the non-orthogonal basis $\{\varphi_m\}_{m=1}^5$ in (3.26). To cope with this, we pre-compute the expansion coeffients $\{a_m\}_{m=1}^5$ using much higher precision, specifically the quadruple precision, and store these coefficients into files. They will be used in the main computer codes which are implemented in double precision. The cost to pre-compute the coefficients is insignificant with respect to the run time of the entire algorithm.

To illustrate the difference in using different precisions to compute the local expansion coefficients $\{a_m\}_{m=1}^5$, we consider a domain in the 1D2V model, with $x_2 \in [0, 10\pi]$, $v_1, v_2 \in [-1.2, 1.2]$, and 80 equally spaced elements along each direction. For the mesh element with index 70 in x_2, index 20 in v_1 and v_2, the coefficients computed with the double precision are

$$a_1 \approx -54382.955, \quad a_2 = 0, \quad a_3 \approx -667.97296, \quad a_4 \approx 464.18641, \quad a_5 \approx 36989.561,$$

while using quadruple computing, we obtain

$$a_1 \approx -54382.948, \quad a_2 = 0, \quad a_3 \approx -667.97288, \quad a_4 \approx 464.18635, \quad a_5 \approx 36989.557.$$

One can observe that only 6 significant digits can be computed accurately if double precision is used to get these coefficients.

For $\mathcal{G}_h^{+2}$, the situation is similar. We will use orthogonal basis for each mesh element, and pre-compute and store the expansion coefficients in the expression of each basis function. Compared with $\mathcal{G}_h^{+1}$, there are many more coefficients to compute. This fact can cause additional loss of significant digits when computing the total mass and total energy due to roundoff errors. For example, to compute the total mass, the element-wise contribution is $\int_K f_h dx_2 dv_1 dv_2 =$

$\sum_{m=1}^{11} f_{h,K}^m \int_K \phi_m dx_2 dv_1 dv_2$. Our numerical experiments show that it is important to pre-compute $\int_K \phi_m dx_2 dv_1 dv_2$, $\forall m = 1, \ldots, 11, \forall K \in T_h$ using quadruple precision to reduce the loss of significance. Similar consideration is also taken into account when the total energy is computed.

5 Numerical Experiments

In this section, we demonstrate the performance of our proposed DG methods using two benchmark examples, streaming Weibel instability and wakefield acceleration. Although our schemes in principle can be applied to the RVM system of general dimensions, we here only present numerical results for a reduced model: 1D2V case, with the obvious reason in computational complexity. With 1D2V, we refer to the RVM system defined for one spatial variable x_2 and two velocity variables v_1 and v_2. In this case, the particle number density function is in the form $f(x_2, v_1, v_2, t)$, while electric and magnetic fields are given by $E = (E_1(x_2, t), E_2(x_2, t), 0)$ and $B = (0, 0, B_3(x_2, t))$, respectively. The reduced RVM system (without the divergence equations) becomes

$$\begin{cases} \partial_t f + \dfrac{v_2}{\sqrt{1+v_1^2+v_2^2}} \partial_{x_2} f + \left(E_1 + \dfrac{v_2 B_3}{\sqrt{1+v_1^2+v_2^2}} \right) \partial_{v_1} f + \left(E_2 - \dfrac{v_1 B_3}{\sqrt{1+v_1^2+v_2^2}} \right) \partial_{v_2} f = 0, \\ \partial_t E_1 = \partial_{x_2} B_3 - J_1, \quad \partial_t E_2 = -J_2, \quad \partial_t B_3 = \partial_{x_2} E_1, \end{cases} \tag{5.53}$$

with

$$J_1(x_2, t) = \int_{\Omega_v} \frac{f v_1}{\sqrt{1+v_1^2+v_2^2}} dv_1 dv_2, \quad J_2(x_2, t) = \int_{\Omega_v} \frac{f v_2}{\sqrt{1+v_1^2+v_2^2}} dv_1 dv_2. \tag{5.54}$$

5.1 Accuracy tests

In this subsection, the accuracy of the proposed DG methods (using $\mathcal{G}_h^k$ and $\mathcal{G}_h^{+k}$) will be tested. We start with reviewing an important feature of the RVM system, the time reversibility property: *Let the exact solution of the RVM system be $f(x, v, t)$, $E(x, t)$, $B(x, t)$ at time t. If the initial conditions are set to be $f(x, -v, T)$, $E(x, T)$, $-B(x, T)$, then the exact solution at time T will be $f(x, -v, 0)$, $E(x, 0)$, $-B(x, 0)$.* We will utilize this property to compute the errors and convergence orders of the numerical solutions. The initial conditions are set to be

$$\begin{cases} f(x_2, v_1, v_2, 0) = \dfrac{1}{\pi\beta} e^{-v_2^2/\beta} [\delta e^{-(v_1 - v_{0,1})^2/\beta} + (1-\delta) e^{-(v_1 + v_{0,2})^2/\beta}], \\ E_1(x_2, v_1, v_2, 0) = E_2(x_2, v_1, v_2, 0) = 0, B_3(x_2, v_1, v_2, 0) = b \sin(k_0 x_2), \end{cases} \tag{5.55}$$

where $\beta = 0.01$, $\delta = 0.5$, $b = 0.001$, $k_0 = 0.2$ and $v_{0,1} = v_{0,2} = 0.3$. The computational domain is $\Omega_x = [0, L_y]$ with $L_y = 2\pi/k_0$, and $\Omega_v = [-2.4, 2.4]^2$. The initial mesh is generated from uniformly partitioning the domain into $20 \times 20 \times 20$ cubes, and then the mesh is further refined twice uniformly. In the numerical simulation, we run the code to $T = 5$, and then use $f_h(x_2, -v_1, -v_2, T = 5)$, $E_h(x_2, T = 5)$ and $-B_h(x_2, T = 5)$ as the initial conditions to run the simulation to $T' = 5$. The resulted numerical solutions will be compared with the initial data (5.55) to calculate the errors and convergence orders.

We consider three numerical fluxes for the Maxwell solver, with the CFL number $C_{cfl} = 0.39$ for the upwind and central fluxes and $C_{cfl} = 0.25$ for the alternating flux when $k = 1$. Here the CFL number is used to dynamically determine the time step Δt_n,

$$\Delta t_n = C_{cfl} \frac{\Delta x}{\max_\Omega \left(\frac{|v_2|}{\sqrt{1+v_1^2+v_2^2}}, \left| E_1 + \frac{v_2 B_3}{\sqrt{1+v_1^2+v_2^2}} \right|, \left| E_2 - \frac{v_1 B_3}{\sqrt{1+v_1^2+v_2^2}} \right| \right)}, \tag{5.56}$$

and $\Delta x = \min(h_{x_2}, h_{v_1}, h_{v_2})$. When $k = 2$, we take $C_{cfl} = 0.19$ for the upwind and central fluxes, and $C_{cfl} = 0.1$ for the alternating flux. When $k = 3$, for the initial 20^3 mesh, we take $C_{cfl} = 0.1$ for upwind and central fluxes, and $C_{cfl} = 0.06$ for the alternating flux. When the mesh is further refined, we hope to have $\Delta t = O(\Delta x^{\frac{4}{3}})$ so the accuracy due to temporal and phase discretizations will be comparable. This can be achieved by reducing the value of C_{cfl} along with the mesh refinement. For instance, from the 20^3 mesh to the next 40^3 mesh, the CFL number can be reduced by a factor of $2^{4/3}$. It is observed that the same CFL numbers that are good for standard DG methods work for the enriched DG methods (with the same index k).

In Tables 5.1 - 5.3, L^2 errors and convergence orders are presented for standard DG methods, with the numerical fluxes in Maxwell solver being upwind, central, and alternating, respectively. Note that the errors in f are essentially independent of the numerical fluxes in Maxwell solver. So are the ones for E_2. Overall with the upwind and alternating fluxes, we observe the optimal $(k+1)^{th}$ order of convergence when $\mathcal{G}_h^k \times \mathcal{U}_h^k \times \mathcal{U}_h^k, k = 1, 2, 3$ are used as the discrete spaces; while with the central fluxes in Maxwell solver, the methods are observed to be k^{th} order accurate in E_1 and B_3 for odd value $k = 1$. This is known for central fluxes in wave simulations. Here the optimal accuracy is with respect to the best approximation properties of the discrete spaces.

		f		E_1		E_2		B_3	
Upwind	h	2.617E-1	-	2.267E-6	-	1.440E-5	-	3.705E-6	-
	$\frac{h}{2}$	8.989E-2	1.542	9.597E-7	1.240	5.551E-7	4.692	8.117E-7	5.512
	$\frac{h}{4}$	2.543E-2	1.822	1.840E-7	2.383	1.290E-7	2.105	1.759E-7	2.206
Central	h	2.617E-1	-	1.982E-6	-	1.395E-5	-	1.504E-5	-
	$\frac{h}{2}$	8.989E-2	1.542	1.110E-6	0.836	5.165E-7	4.755	9.262E-6	0.699
	$\frac{h}{4}$	2.543E-2	1.822	5.776E-7	0.942	1.187E-7	2.121	5.363E-6	0.788
Alternating	h	2.617E-1	-	3.199E-7	-	1.453E-5	-	3.951E-6	-
	$\frac{h}{2}$	8.989E-2	1.542	1.994E-8	4.004	5.553E-7	4.710	1.065E-6	1.891
	$\frac{h}{4}$	2.543E-2	1.822	2.759E-9	2.853	1.290E-7	2.106	2.901E-7	1.876

Table 5.1: L^2 errors and orders of the standard DG methods with $\mathcal{G}_h^k \times \mathcal{U}_h^k \times \mathcal{U}_h^k$, $k = 1$. Upwind, central, and alternating fluxes are used in the Maxwell solver.

		f		E_1		E_2		B_3	
Upwind	h	1.327E-1	-	1.548E-7	-	3.781E-7	-	6.052E-7	-
	$\frac{h}{2}$	2.858E-2	2.215	3.328E-8	2.218	1.933E-7	0.968	6.076E-8	3.316
	$\frac{h}{4}$	3.927E-3	2.863	2.233E-9	3.898	1.843E-8	3.391	6.316E-9	3.266
Central	h	1.327E-1	-	8.196E-8	-	3.781E-7	-	6.322E-7	-
	$\frac{h}{2}$	2.858E-2	2.215	1.154E-9	6.150	1.933E-7	0.968	6.310E-8	3.325
	$\frac{h}{4}$	3.927E-3	2.863	6.999E-11	4.043	1.844E-8	3.390	6.327E-9	3.318
Alternating	h	1.327E-1	-	9.465E-8	-	3.814E-7	-	4.678E-7	-
	$\frac{h}{2}$	2.858E-2	2.215	1.790E-9	2.403	1.933E-7	0.981	6.497E-8	2.848
	$\frac{h}{4}$	3.927E-3	2.863	9.584E-11	4.223	1.844E-8	3.390	3.951E-9	4.040

Table 5.2: L^2 errors and orders of the standard DG methods with $\mathcal{G}_h^k \times \mathcal{U}_h^k \times \mathcal{U}_h^k$, $k = 2$. Upwind, central, and alternating fluxes are used in the Maxwell solver.

For the enriched DG methods with $\mathcal{G}_h^{+k} \times \mathcal{U}_h^k \times \mathcal{U}_h^k, k = 0, 1, 2$, the errors and convergence orders

		f		E_1		E_2		B_3	
Upwind	h	7.079E-2	-	8.498E-8	-	6.536E-7	-	8.396E-7	-
	$\frac{h}{2}$	6.372E-3	3.473	5.217E-9	4.026	1.335E-8	5.614	1.736E-8	5.596
	$\frac{h}{4}$	5.375E-4	3.567	9.131E-11	5.836	7.768E-10	4.103	1.084E-9	4.001
Central	h	7.079E-2	-	1.177E-7	-	6.481E-7	-	8.118E-7	-
	$\frac{h}{2}$	6.372E-3	3.473	1.214E-8	3.277	1.336E-8	5.600	9.536E-8	3.090
	$\frac{h}{4}$	5.375E-4	3.567	6.659E-10	4.188	7.767E-10	4.104	2.628E-9	5.181
Alternating	h	7.079E-2	-	4.304E-8	-	6.532E-7	-	8.704E-7	-
	$\frac{h}{2}$	6.372E-3	3.473	1.228E-9	5.131	1.334E-8	5.614	1.893E-8	5.523
	$\frac{h}{4}$	5.375E-4	3.567	1.315E-11	6.545	7.768E-10	4.102	1.053E-9	4.168

Table 5.3: L^2 errors and orders of the standard DG methods with $\mathcal{G}_h^k \times \mathcal{U}_h^k \times \mathcal{U}_h^k$, $k = 3$. Upwind, central, and alternating fluxes are used in the Maxwell solver.

of the numerical solutions are reported in Tables 5.4 - 5.6, where again three numerical fluxes are used in Maxwell solver. Similar as in the standard DG methods, we observe optimal accuracy of the enriched DG methods when the upwind and alternating fluxes are used in Maxwell solver, and the accuracy becomes suboptimal in E_1 and B_3 when the scheme uses the central flux and $k = 1$. The errors in f and in E_2 are not sensitive to the different numerical fluxes in Maxwell solver. When $k = 0$, we take $C_{cfl} = 1.2$ for the upwind and central fluxes, and $C_{cfl} = 0.9$ for the alternating flux. Even though there is no theoretical error estimate available for the case of $k = 0$, overall first order convergence rate is observed.

If we compare the standard and enriched DG methods for $k = 1, 2$, it is observed that the enriched DG methods produce more accurate f, which is not a surprise given $\mathcal{G}_h^k \subset \mathcal{G}_h^{+k}$.

		f		E_1		E_2		B_3	
Upwind	h	3.806E-1	-	7.261E-6	-	1.321E-4	-	1.829E-4	-
	$\frac{h}{2}$	2.194E-1	0.795	2.172E-6	1.741	4.356E-5	1.601	1.072E-4	0.771
	$\frac{h}{4}$	1.014E-1	1.113	1.301E-6	0.739	2.547E-5	0.774	5.340E-5	1.005
Central	h	3.806E-1	-	2.278E-5	-	1.533E-4	-	6.910E-5	-
	$\frac{h}{2}$	2.194E-1	0.795	2.888E-6	2.980	4.698E-5	1.706	3.284E-5	1.075
	$\frac{h}{4}$	1.014E-1	1.113	9.615E-7	1.587	2.645E-5	0.829	1.615E-5	1.024
Alternating	h	3.806E-1	-	1.513E-5	-	1.207E-4	-	6.834E-5	-
	$\frac{h}{2}$	2.194E-1	0.795	2.510E-6	2.592	4.718E-5	1.355	3.254E-5	1.071
	$\frac{h}{4}$	1.014E-1	1.113	9.361E-7	1.423	2.653E-5	0.831	1.613E-5	1.013

Table 5.4: L^2 errors and orders of the enriched DG methods with $\mathcal{G}_h^{+k} \times \mathcal{U}_h^k \times \mathcal{U}_h^k$, $k = 0$. Upwind, central, and alternating fluxes are used in the Maxwell solver.

5.2 Conservation and long time behavior: streaming Weibel instability

In this subsection, we will investigate the performance of the proposed methods in terms of conservation and long time behavior through the streaming Weibel instability. Streaming Weibel instability was analyzed in [16, 3, 5] in non-relativistic or relativistic setting. It is driven by the anisotropy in velocity space, and a small perturbation initially in the magnetic field will cause the

		f		E_1		E_2		B_3	
Upwind	h	2.552E-1	-	1.643E-6	-	9.148E-6	-	3.628E-6	-
	$\frac{h}{2}$	7.477E-2	1.771	9.746E-7	0.754	2.186E-7	5.387	8.019E-7	2.178
	$\frac{h}{4}$	2.044E-2	1.871	1.859E-7	2.390	4.996E-8	2.129	1.748E-7	2.198
Central	h	2.552E-1	-	3.385E-6	-	8.769E-6	-	1.538E-5	-
	$\frac{h}{2}$	7.477E-2	1.771	9.727E-7	1.799	2.127E-7	5.366	9.431E-6	0.706
	$\frac{h}{4}$	2.044E-2	1.871	5.466E-7	0.832	4.671E-8	2.187	5.407E-6	0.803
Alternating	h	2.552E-1	-	3.487E-7	-	9.254E-6	-	3.588E-6	-
	$\frac{h}{2}$	7.477E-2	1.771	2.156E-8	4.016	2.197E-7	5.397	1.075E-6	1.739
	$\frac{h}{4}$	2.044E-2	1.871	2.119E-9	3.347	5.002E-8	2.135	2.916E-7	1.882

Table 5.5: L^2 errors and orders of the enriched DG methods with $\mathcal{G}_h^{+k} \times \mathcal{U}_h^k \times \mathcal{U}_h^k$, $k = 1$. Upwind, central, and alternating fluxes are used in the Maxwell solver.

		f		E_1		E_2		B_3	
Upwind	h	5.711E-2	-	1.603E-7	-	2.673E-7	-	5.971E-7	-
	$\frac{h}{2}$	6.720E-3	3.087	3.402E-8	2.236	1.964E-7	0.445	6.117E-8	3.287
	$\frac{h}{4}$	8.660E-4	2.956	2.228E-9	3.933	1.837E-8	3.418	6.314E-9	3.276
Central	h	5.711E-2	-	8.933E-8	-	2.670E-7	-	6.281E-7	-
	$\frac{h}{2}$	6.720E-3	3.087	1.399E-9	5.997	1.964E-7	0.443	6.372E-8	3.301
	$\frac{h}{4}$	8.660E-4	2.956	6.667E-11	4.391	1.838E-8	3.418	6.324E-9	3.333
Alternating	h	5.712E-2	-	1.039E-7	-	2.670E-7	-	4.629E-7	-
	$\frac{h}{2}$	6.720E-3	3.088	2.156E-9	5.591	1.965E-7	0.442	6.665E-8	2.796
	$\frac{h}{4}$	8.660E-4	2.956	9.685E-11	4.477	1.838E-8	3.418	3.944E-9	4.079

Table 5.6: L^2 errors and orders of the enriched DG methods with $\mathcal{G}_h^{+k} \times \mathcal{U}_h^k \times \mathcal{U}_h^k$, $k = 2$. Upwind, central, and alternating fluxes are used in the Maxwell solver.

growth of the electromagnetic energy over time. The problem is set up by taking the same initial conditions and the computational domain as in Section 5.1 for the accuracy tests.

We will start with the standard DG method using $\mathcal{G}_h^1 \times \mathcal{U}_h^1 \times \mathcal{U}_h^1$ on an 80^3 uniform mesh, where the numerical fluxes in Maxwell solver are upwind, central, or alternating. In Figure 5.1, the time history of the relative error in the conservation quantities, i.e. total mass and energy, is plotted. The relative error at time t is defined with respect to the initial value at time 0. Since our simulation is carried out in double precision, the total mass is preserved perfectly with a relative error of the magnitude 10^{-14} over a long period of time. The relative error in the total energy is on the scale of 10^{-4} for upwind flux (see top row), and it is smaller for the central and alternating fluxes and is around 10^{-5}. Upwind flux in Maxwell solver will contribute to additional numerical dissipation which is in the form of I_2 in Theorem 3.3. We want to mention it is important to choose large enough domain in velocity direction to eliminate the boundary effect in conservation. For example, if the velocity domain is taken to be half of the size, namely, the computational domain is $[0, 10\pi] \times [-1.2, 1.2] \times [-1.2, 1.2]$, and if the mesh spacing stays unchanged, the relative error in the total mass of the computed solutions will be around 10^{-7}.

In Figure 5.2, we plot the time evolution of electric and magnetic energy of the numerical solutions, using upwind flux (top left), central flux (top right) and alternating flux (bottom) in the Maxwell solver. The electric and magnetic energy are defined as $\frac{1}{2}\int_{\Omega_x}(E_1^2+E_2^2)dx_2$ and $\frac{1}{2}\int_{\Omega_x} B_3^2 dx_2$,

respectively. The long time dynamics of the electric and magnetic energy is not sensitive to the choice of the upwind or central numerical fluxes with the same CFL number. There is slight difference at initial stage when the alternating flux is used for the Maxwell solver with a different CFL number. Nevertheless, in all cases, the exponential growth is well captured in each energy along with the development of instability.

Next, we consider the enriched DG method using $\mathcal{G}_h^{+1} \times \mathcal{U}_h^1 \times \mathcal{U}_h^1$ on an 80^3 uniform mesh, where the numerical fluxes in Maxwell solver are upwind, central or alternating. Our analysis implies that such methods, at least in their semi-discrete forms, will conserve energy over time when central or alternating flux is used in Maxwell solver, while the method with upwind flux in Maxwell solver will have additional energy dissipation. The total mass again is preserved perfectly with machine accuracy level relative errors, and the results are not reported. In Figure 5.3, the time history of the relative error in total energy is plotted for the numerical solutions, which are computed with upwind flux (top row), central flux (middle row), and alternating flux (bottom row). With the upwind flux, the relative error of total energy is of the magnitude 10^{-5}, which is smaller than that from the standard upwind DG method, see Figure 5.1. With the central flux, the relative error of total energy at $T = 100$ is -4.5×10^{-8}, much better than the enriched DG method using upwind flux and the standard DG method with $k = 1$. This is consistent to our theoretical understanding. On the other hand, this error in the total energy with the central flux is much larger than the machine epsilon. This does not contradict with the result in Theorem 3.3 which is for semi-discrete enriched DG methods. The error we observed in the total energy mainly comes from the temporal discretization, which is dissipative and does not conserve energy. Evidence can be seen from the middle row of the plot in Figure 5.3, where the CFL number is reduced by half and the energy conservation is improved. The numerical solutions with alternating flux perform similarly as with central fluxes in energy conservation.

We now turn to the simulations by standard and enriched DG methods using $\mathcal{G}_h^k$ and $\mathcal{G}_h^{+k}$, $k = 2$. In Figure 5.4, the time history of the relative error in total energy is plotted for the standard DG (left column) and enriched DG method (right column). In the top row, central flux is used with $C_{cfl} = 0.19$, while alternating flux is used in the bottom row with $C_{cfl} = 0.1$. In all cases, the errors in total energy are in comparable magnitude, and they are also comparable with the results by the enriched DG method with $k = 1$, see Figure 5.3. With enriched spaces, DG methods also produce non-increasing time history of the error of total energy, and this is desired in application.

For completeness, we also examine the conservation property of the enriched DG method using $\mathcal{G}_h^{+0} \times \mathcal{U}_h^0 \times \mathcal{U}_h^0$, which has lower accuracy order than the methods we have discussed in this subsection so far. The mesh is taken to be 80^3 and uniform. Just as in the case $k = 1, 2$, the total mass is preserved perfectly with the relative error at the machine accuracy level. In Figure 5.5 we report the relative error of the total energy. One can see that the energy is conserved up to the magnitude 10^{-3} when the upwind flux is used in the Maxwell solver, and it is around 10^{-9} with the central or alternating flux. Compared with the enriched DG method with $k = 1, 2$, the method with $k = 0$ produces larger errors in the early stage, for instance when $T < 40$.

To better illustrate the various methods in conserving energy, we collect the relative errors of the total energy at $T = 20$, 40, 60, 80 and 100 in Table 5.7. Terminology like "$\mathcal{G}_h^{+1} - \text{Upwind} - 0.39$" indicates that $f_h \in \mathcal{G}_h^{+1}$, the upwind numerical flux is used for the Maxwell solver, and the CFL number $C_{cfl} = 0.39$ is taken. The first observation is that with the upwind flux (see row 1), the energy conservation deteriorates the fastest over time, and this reflects the dissipative nature of the upwind flux in Maxwell solver. Among all the cases using central flux, the $\mathcal{G}_h^{+1} - \text{Central} - 0.19$ displays the best conservation property at the selected discrete times. Particularly, it is slightly better than $\mathcal{G}_h^{+2}-\text{Central}-0.19$. This can be explained that the space $\mathcal{G}_h^{+2}$ involves 11 basis functions in each mesh element, while $\mathcal{G}_h^{+1}$ involves 5, and hence the former can suffer more in roundoff errors, see discussion in Section 4. When comparing the performance in energy conservation between

$\mathcal{G}_h^{+2}-$ Central $-$ 0.19 and $\mathcal{G}_h^2-$ Central $-$ 0.19, we can see that $\mathcal{G}_h^{+2}-$ Central $-$ 0.19 performs better at $T = 20$, 40, 60 and 80, yet not at $T = 100$. Even though there is no provable energy conservation property for standard DG method with $\mathcal{G}_h^2$, the method indeed preserve the total energy quite well over time. We attribute this to that higher order polynomial spaces can better approximate the non-polynomial function $\sqrt{1+|v|^2}$, hence lead to better performance in conserving energy of the standard DG methods. When the alternating flux is used, the energy conservation of $\mathcal{G}_h^{+1}-$ Alternating $-$ 0.19 is comparable and indeed slightly better than $\mathcal{G}_h^{+1}-$ Central $-$ 0.19. When we compare $\mathcal{G}_h^{+2}-$ Alternating $-$ 0.1 and $\mathcal{G}_h^2-$ Alternating $-$ 0.1, it is easy to see that $\mathcal{G}_h^{+2}$ outperforms $\mathcal{G}_h^2$ at all the given discrete times.

	$T=20$	$T=40$	$T=60$	$T=80$	$T=100$
$\mathcal{G}_h^{+1}-$ Upwind $-$ 0.39	-4.9E-11	-3.8E-10	-5.8E-09	-1.8E-06	-4.2E-05
$\mathcal{G}_h^{+1}-$ Central $-$ 0.39	-3.7E-11	-7.1E-11	-9.8E-11	1.9E-10	-4.3E-08
$\mathcal{G}_h^{+1}-$ Central $-$ 0.19	-1.5E-12	-3.8E-12	-9.8E-12	2.1E-11	-5.0E-09
$\mathcal{G}_h^{+2}-$ Central $-$ 0.19	-4.8E-12	-9.0E-12	-1.2E-11	3.7E-11	-1.0E-08
$\mathcal{G}_h^2-$ Central $-$ 0.19	4.3E-11	2.3E-10	7.6E-10	1.8E-09	-5.2E-09
$\mathcal{G}_h^{+1}-$ Alternating $-$ 0.19	-1.6E-12	-3.8E-12	-9.8E-12	1.8E-11	-4.8E-09
$\mathcal{G}_h^{+2}-$ Alternating $-$ 0.1	-8.5E-13	-1.5E-12	-1.9E-12	5.3E-12	-1.5E-09
$\mathcal{G}_h^2-$ Alternating $-$ 0.1	4.7E-11	2.4E-10	7.7E-10	1.8E-09	3.7E-09

Table 5.7: Relative errors of the total energy for the proposed methods under different settings at selected discrete times.

To summarize, the enriched DG methods with $\mathcal{G}_h^{+1}$ or $\mathcal{G}_h^{+2}$ lead to much better energy conservation compared with the standard DG method with $\mathcal{G}_h^1$. Overall the enriched DG method with $\mathcal{G}_h^{+2}$ does not necessarily outperform $\mathcal{G}_h^{+1}$ greatly. Our observations imply that for relatively lower order methods, enriched DG methods are more advantageous in conserving the total energy, while for high order methods, standard DG methods can do well in energy conservation, without the ill-conditioning issue associated with the added non-polynomial function in the enriched DG methods.

5.3 Wakefield Acceleration

In this example, we consider the laser wakefield acceleration, where an electromagnetic wave, such as a laser or a light pulse, is emitted to a stationary plasma, the plasma particles will then be excited to accelerate [20, 21]. To specify boundary conditions for electromagnetic fields, we first note that the Maxwell part of the equations (5.54) can be rewritten in their characteristic variables, namely

$$\begin{cases} \dfrac{\partial}{\partial t}\left(E_1+B_3\right)-\dfrac{\partial}{\partial x_2}\left(E_1+B_3\right)=-J_1, \\ \dfrac{\partial}{\partial t}\left(E_1-B_3\right)+\dfrac{\partial}{\partial x_2}\left(E_1-B_3\right)=-J_1. \end{cases} \tag{5.57}$$

To model the laser or light pulse entering the domain only from the left boundary, we impose the inflow boundary condition at the left boundary: $E_1 - B_3 = 2G(t)$, where

$$G(t)=A_0 w_L \exp\left(-\frac{(t-2\tau)^2}{\tau^2}\right)\sin(w_L t)$$

with $A_0 = w_L = 2$ and $\tau = \frac{\pi}{2}$. For the right boundary, zero inflow condition is considered by imposing $E_1 + B_3 = 0$. For the particle number density function f, outflow boundary conditions

are used in x_2 direction. This allows particles to leave the spatial domain. In v direction, compact support is assumed for f, and this can be ensured by a sufficiently large velocity domain. At time $t = 0$, we consider a stationary plasma and take $f(x_2, v_1, v_2, 0) = \delta(v_1)\delta(v_2)$, where $\delta(\cdot)$ is Dirac-delta function. The initial electric and magnetic fields are zero. In our implementation, we approximate the delta function using a piecewise constant function in velocity direction. That is, in the mesh element which contains $v_1 = v_2 = 0$, f is approximated by $f_h = 1/(\Delta v_1 \Delta v_2)$; elsewhere, it is approximated by zero.

What we need to decide first is how to truncate the velocity domain Ω_v. A good choice depends on the final time T, which is set to be $T = 10$ in our numerical study. This leads us to take $\Omega_v = [-25, 25] \times [-10, 30]$ in our simulation. The spatial domain, on the other hand, is $\Omega_x = [0, 25]$. We implement the standard DG method with $k = 1$ and the upwind flux in the Maxwell solver. A uniform mesh of $80 \times 81 \times 82$ is used, together with $C_{cfl} = 0.39$. With such choice of the mesh, the delta function in the initial data can be approximated compactly over one mesh element. In order to better visualize the numerical solution which is of high dimensional, we plot the logarithm of v_1-integrated number density function, i.e. $\int f_h dv_1$ in Figure 5.6. It turns out the computed f_h can be negative at some spatial point, so what we actually plot here is $\max(\int f_h dv_1, \epsilon)$, $\epsilon = 10^{-16}$ in the logarithmic scale. The strip pattern observed in Figure 5.6 is due to the presence of negative value for f_h, and the pattern propagates rightward. Despite of this oscillatory behavior in the computed solution, one can clearly observe that the initially stationary particles are accelerated by the emitted electromagnetic wave from the left domain boundary. Till $T = 10$, the spatial region where the particles are affected is about $x_2 \in [0, 13]$. Within this region, most of the particles have been accelerated along the positive v_2 direction.

Although the acceleration of particles can be captured in Figure 5.6, the computed solution f_h is negative in some region hence the numerical solutions are not physical. Moreover, for this particular example, the maximum velocity achieved by the accelerated particles can not be predicted accurately. To overcome this, we apply to f_h the positivity-preserving limiter developed in [25]. To be more specific, let $S_i^{x_2}$ denote a collection of the Gauss quadrature points on the i^{th} element in x_2 direction, and similarly we introduce $S_j^{v_1}$ and $S_l^{v_2}$; let $\hat{S}_i^{x_2}$ denote the Gauss-Lobatto quadrature points on the i^{th} element in x_2 direction, and similarly we introduce $\hat{S}_j^{v_1}$ and $\hat{S}_l^{v_2}$. Define a new set S_{ijl},

$$S_{ijl} = (S_i^{x_2} \otimes S_j^{v_1} \otimes S_l^{v_2}) \cup (\hat{S}_i^{x_2} \otimes S_j^{v_1} \otimes S_l^{v_2}) \cup (S_i^{x_2} \otimes \hat{S}_j^{v_1} \otimes S_l^{v_2}) \cup (S_i^{x_2} \otimes S_j^{v_1} \otimes \hat{S}_l^{v_2}). \quad (5.58)$$

The positivity-preserving limiter is applied element by element as follows. Before each inner stage of the TVD-RK time integration, on each element with index (i, j, l), we modify f_h into $\tilde{f}_h = \theta(f_h - \bar{f}_h) + \bar{f}_h$, with $\bar{f}_h$ be the average of f_h over this element, and $\theta = \min_{(x_2,v_1,v_2)\in S_{i,j,l}}\{1, \frac{\bar{f}_h}{|\bar{f}_h - f_h(x_2,v_1,v_2)|}\}$. In our simulations, we use two and three Gauss quadrature points for $f_h \in \mathcal{G}_h^1$ and $\mathcal{G}_h^2$, respectively, and use three Gauss-Lobatto quadrature points for both cases, which requires the CFL number to be at most $\frac{1}{6}$ (see [25]). Specifically, we choose $C_{cfl} = 0.16$ for simulations using both $\mathcal{G}_h^1$ and $\mathcal{G}_h^2$ discrete spaces with positivity-preserving limiter. In Figure 5.7, we plot the logarithm of v_1-integrated number density function, computed from standard DG method with $k = 1$ (top) and $k = 2$ (bottom), combined with the positivity-preserving limiter. The results are much better than that in Figure 5.6. Moreover, the maximum velocity achieved by the accelerated particles are much higher. When we compare the P^1 result on $80 \times 81 \times 82$ mesh with that on $100 \times 101 \times 102$ mesh, or with the P^2 result on the same $80 \times 81 \times 82$ mesh, the convergence of the main features in the solutions is observed. This confirm what we have seen here is physical. Note that with the positivity preserving technique, the methods still conserves mass yet generally will no longer preserve energy. Hence we choose not to present the computed results using enriched DG methods.

6 Concluding Remarks

In this paper, we propose discontinuous Galerkin (DG) methods for the relativistic Vlasov-Maxwell system. Standard and enriched discrete spaces are used, with the aim to achieve provable energy-conserving schemes. Stability and error estimates are established, together with the conservation properties of the methods. For the enriched space, inverse inequalities and approximation properties are obtained in order to complete the error estimates. Issues in implementing the enriched DG methods are particularly addressed for better numerical stability. All the analytical results are established for semi-discrete methods. When the methods are coupled with the third order TVD Runge-Kutta time discretization, error estimates can be pursued by following similar analysis in [22], which is for standard DG methods solving Vlasov-Maxwell equations. Even though the enriched DG methods using central or alternating numerical fluxes in Maxwell solver are proved to be energy conserving, such properties will not hold completely once the third order TVD Runge-Kutta method is applied in time. For energy-conserving fully-discrete DG methods for the relativistic Vlasov-Maxwell equations, one should apply energy-conserving temporal discretizations, see examples in [4].

References

[1] B. Ayuso, S. Hajian, High order and energy preserving discontinuous Galerkin methods for the Vlasov-Poisson system, preprint, 2012.

[2] C. K. Birdsall and A. B. Langdon, Plasma Physics Via Computer Simulation, McGraw-Hill, New York, 1985.

[3] F. Califano, F. Pegoraro, S. V. Bulanov and A. Mangeney, Kinetic saturation of the Weibel instability in a collisionless plasma, Phys. Rev. E, 57(6):7048-7059, 1998.

[4] Y. Cheng, A. J. Christlieb and X. Zhong, Energy-conserving discontinuous Galerkin methods for the Vlasov-Maxwell system, J. Comput. Phys., 279(15):145-173, 2014.

[5] Y. Cheng, I. M. Gamba, F. Li and P. J. Morrison, Discontinuous Galerkin schemes for Vlasov-Maxwell system, SIAM J. Numer. Anal., 52(2):1017-1049, 2014.

[6] C. Z. Cheng and G. Knorr, The integration of the Vlasov equation in configuration space, J. Comput. Phys., 22(3):330-351, 1976.

[7] P. Ciarlet, The finite element methods for elliptic problems, North-Holland, Amsterdam, 1975.

[8] B. Cohen, A. Langdon, D. Hewett and R. Procassini, Performance and optimization of direct implicit particle simulation, J. Comput. Phys., 81(1):151-168, 1989.

[9] B. Eliasson, Numerical modelling of the two-dimensional Fourier transformed Vlasov-Maxwell system, J. Comput. Phys., 190(2):501-522, 2003.

[10] B. Eliasson, Numerical simulations of the Fourier-transformed Vlasov-Maxwell system in higher dimensions-theory and applications, Transport Theor. Stat., 39(5):387-465, 2011.

[11] C. Gittelson, R. Hiptmair and I. Perugia, Plane wave discontinuous Galerkin methods, Isaac Newton Institute Preprint Series, 2007.

[12] T. Huttunen, P. Monk and J.P. Kaipio, Computational aspects of the ultra-weak variational formulation, J. Comput. Phys., 182(1):27-46, 2002.

[13] G. Jacobs and J.S. Hesthaven, Implicit-explicit time integration of a high-order particle-in-cell method with hyperbolic divergence cleaning, Comput. Phys. Commun., 180(10):1760-1767, 2009.

[14] A. J. Klimas and W. M. Farrell, A splitting algorithm for Vlasov simulation with filamentation filtration, J. Comput. Phys., 110(1):150-163, 1994.

[15] S. Markidis and G. Lapenta, The energy conserving particle-in-cell method, J. Comput. Phys., 230(18):7037-7052, 2011.

[16] F. Pegoraro, S. V. Bulanov, F. Califano and M. Lontano, Nonlinear development of the Weibel instability and magnetic field generation in collisionless plasmas, Phys. Scripta, T63:262-265, 1996.

[17] J.-M. Qiu and C.-W. Shu, Conservative high order semi-Lagrangian finite difference WENO methods for advection in incompressible flow, J. Comput. Phys., 230(4):863-889, 2011.

[18] C.-W. Shu and S. Osher, Efficient implementation of essentially non-oscillatory shock capturing schemes, J. Comput. Phys., 77(2):439-471, 1988.

[19] E. Sonnendrücker, J. Roche, P. Bertrand and A. Ghizzo, The semi-Lagrangian method for the numerical resolution of the Vlasov equation, J. Comput. Phys., 149(2):201-220, 1999.

[20] A. Suzuki and T. Shigeyama, A conservative scheme for the relativistic Vlasov-Maxwell system, J. Comput. Phys., 229(5):1643-1660, 2010.

[21] H. Yang, Analysis and applications of Runge-Kutta discontinuous Galerkin methods, Ph.D. dissertation, Rensselaer Polytechnic Institute, 2014.

[22] H. Yang and F. Li, Error estimates of Runge-Kutta discontinuous Galerkin methods for the Vlasov-Maxwell system, ESAIM: M2AN, 49(1):69-99, 2015.

[23] S. I. Zaki, L. R. T. Gardner and T. J. M. Boyd, A finite element code for the simulation of one-dimensional Vlasov plasmas. i. theory, J. Comput. Phys., 79(1):184-199, 1988.

[24] S. I. Zaki, T. J. M. Boyd and L. R. T. Gardner, A finite element code for the simulation of one-dimensional Vlasov plasmas. ii. applications, J. Comput. Phys., 79(1):200-208, 1988.

[25] X. Zhang and C.-W. Shu, On maximum-principle-satisfying high order schemes for scalar conservation laws, J. Comput. Phys., 229(9):3091-3120, 2010.

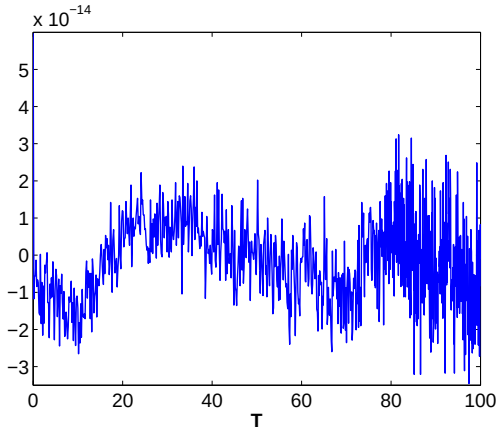

(a) Mass: upwind

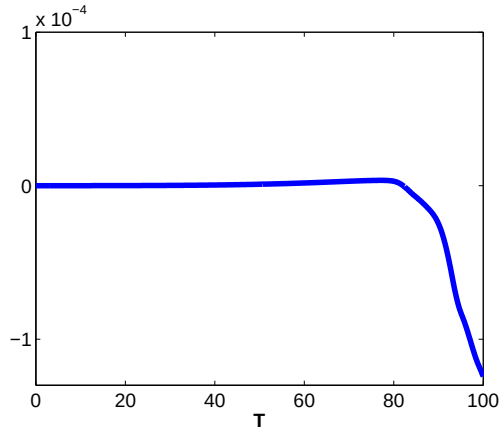

(b) Total energy: upwind

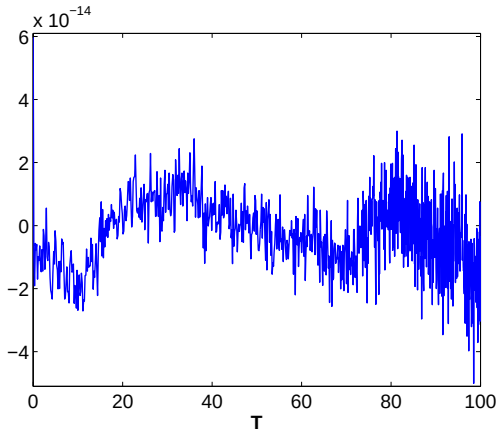

(c) Mass: central

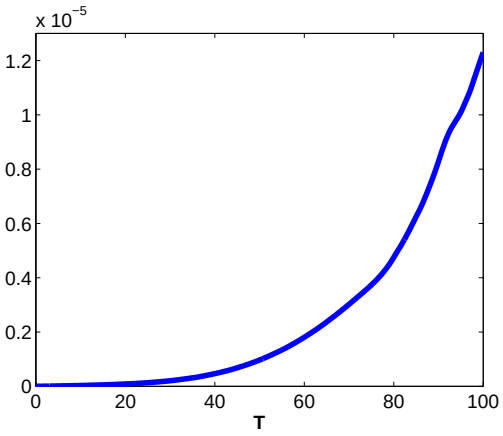

(d) Total energy: central

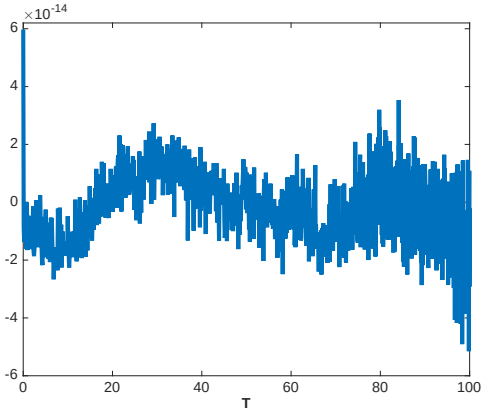

(e) Mass: alternating

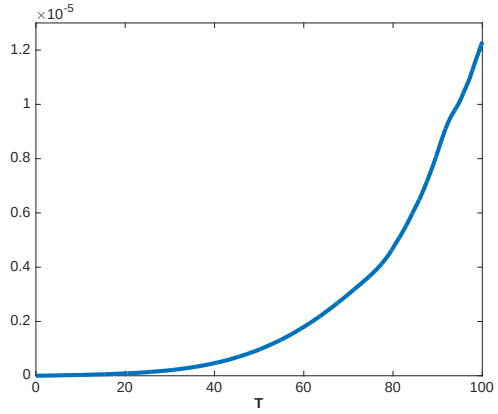

(f) Total energy: alternating

Figure 5.1: Time history of the relative errors in conservation quantities for the streaming Weibel instability. Standard DG methods with $k = 1$. $C_{cfl} = 0.39$ for upwind and central fluxes. $C_{cfl} = 0.25$ for alternating flux.

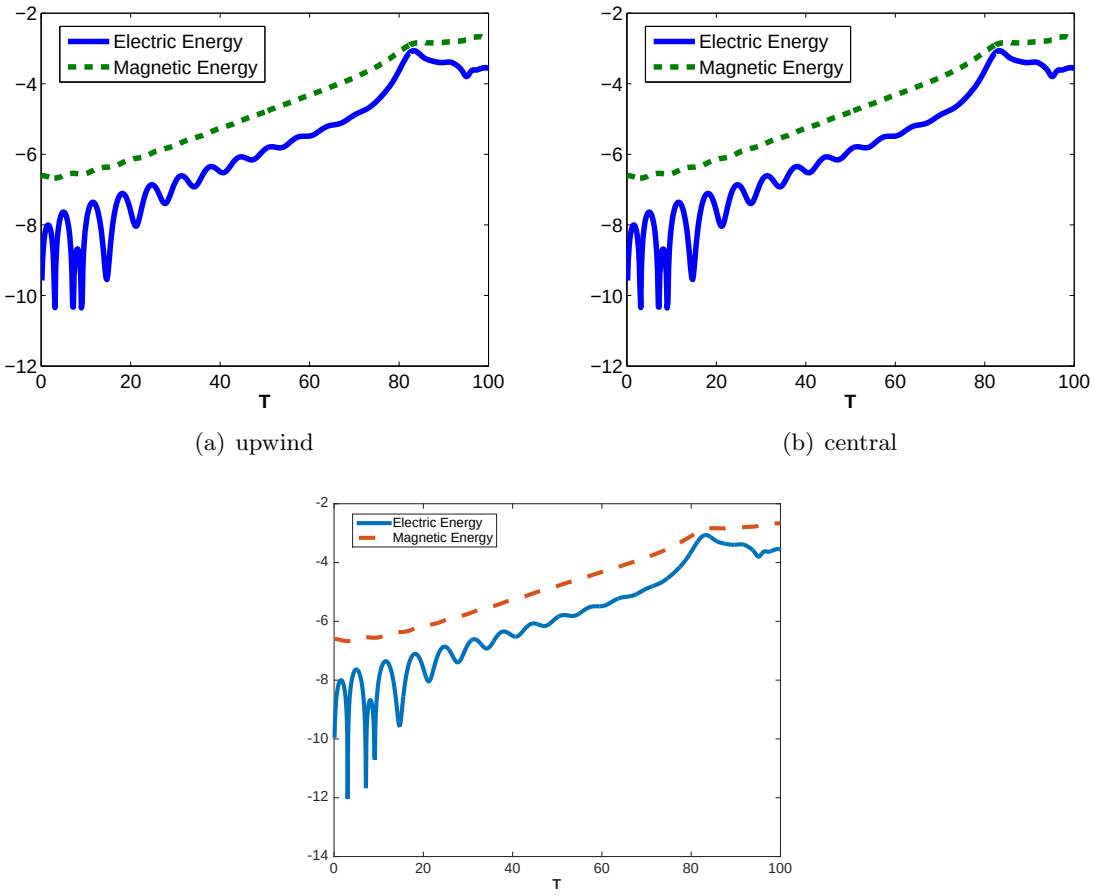

(a) upwind

(b) central

(c) alternating

Figure 5.2: Time evolution of the logarithm of electric and magnetic energy for the streaming Weibel instability. Standard DG method with $\mathcal{G}_h^k$ and $k = 1$. $C_{cfl} = 0.39$ for upwind and central fluxes. $C_{cfl} = 0.25$ for alternating flux.

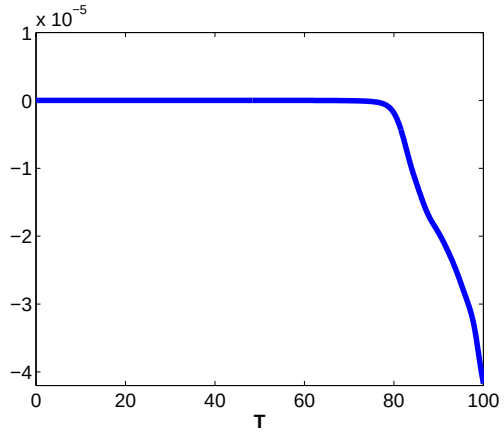

(a) Upwind, $C_{cfl} = 0.39$

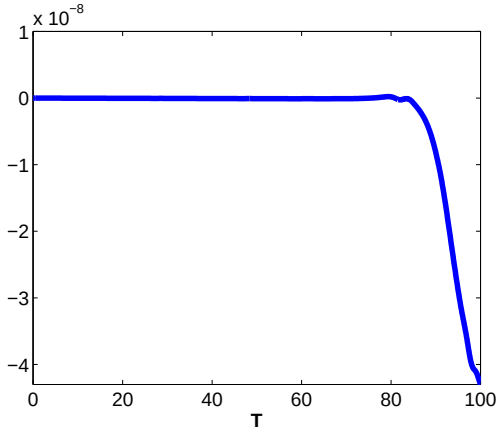

(b) Central, $C_{cfl} = 0.39$

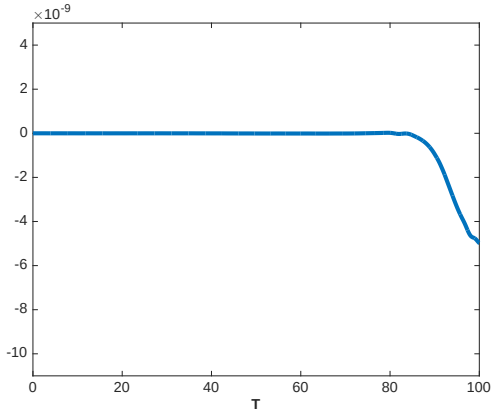

(c) Central, $C_{cfl} = 0.19$

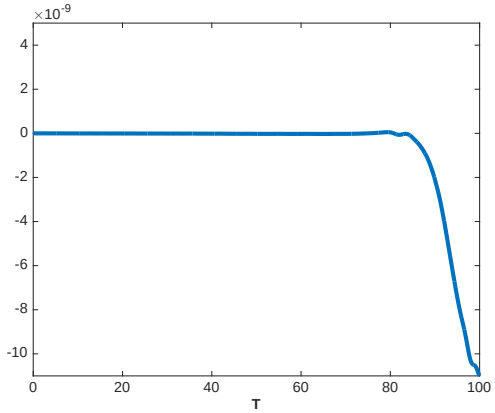

(d) Alternating, $C_{cfl} = 0.25$

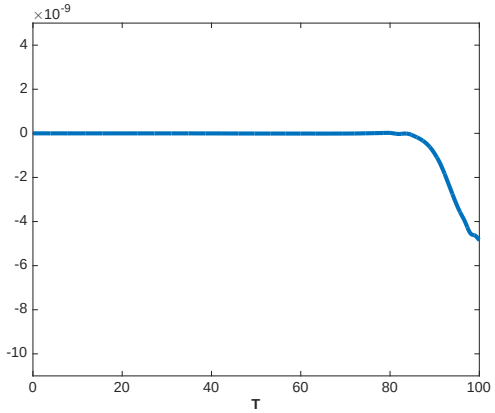

(e) Alternating, $C_{cfl} = 0.19$

Figure 5.3: Time history of the relative error in the total energy for the streaming Weibel instability. Enriched DG methods with $\mathcal{G}_h^{+k}$ and $k = 1$. Three different numerical fluxes in Maxwell solver.

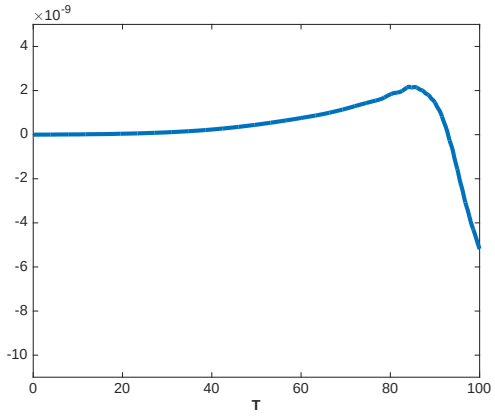

(a) Standard DG with $\mathcal{G}_h^k, k = 2$

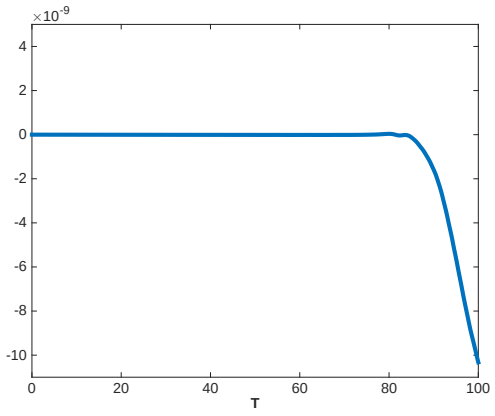

(b) Enriched DG with $\mathcal{G}_h^{+k}, k = 2$

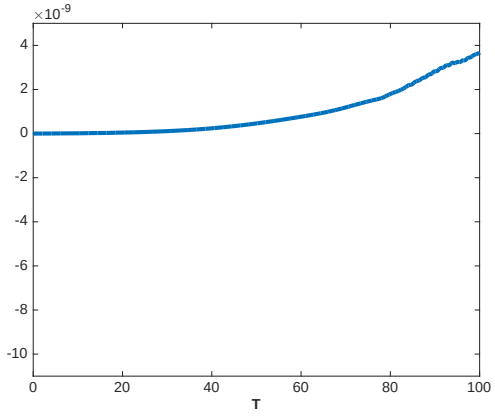

(c) Standard DG with $\mathcal{G}_h^k, k = 2$

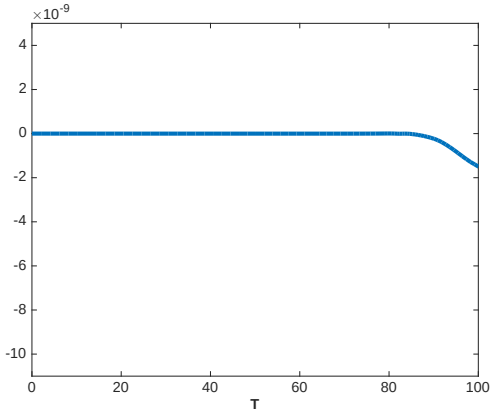

(d) Enriched DG with $\mathcal{G}_h^{+k}, k = 2$

Figure 5.4: Time history of the relative error in the total energy for the streaming Weibel instability. Top: central flux with $C_{cfl} = 0.19$. Bottom: alternating flux with $C_{cfl} = 0.1$.

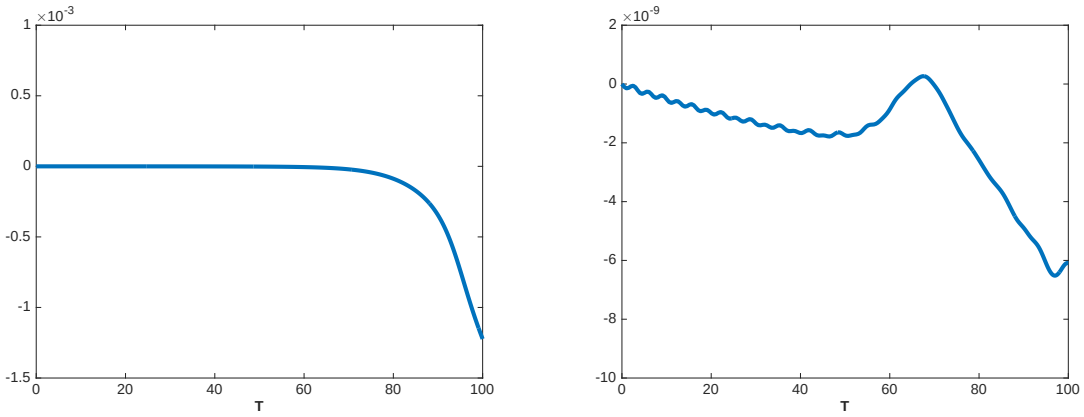

(a) Upwind

(b) Central

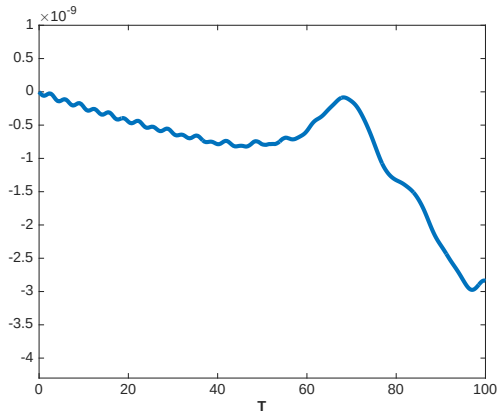

(c) Alternating

Figure 5.5: Time history of the relative error in the total energy for the streaming Weibel instability. Enriched DG method with $\mathcal{G}_h^k$ and $k = 0$. $C_{cfl} = 1.2$ for upwind and central fluxes. $C_{cfl} = 0.9$ for alternating flux.

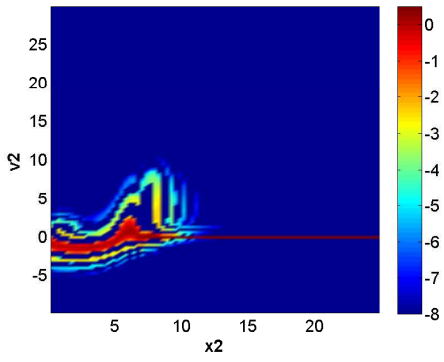

Figure 5.6: Logorithm of the v_1-integrated number density function $\max(\int f_h dv_1, \epsilon)$ with $\epsilon = 10^{-16}$ in the wakefield acceleration example. Standard DG method with G_h^k and $k = 1$. $T = 10$ and $C_{cfl} = 0.39$.

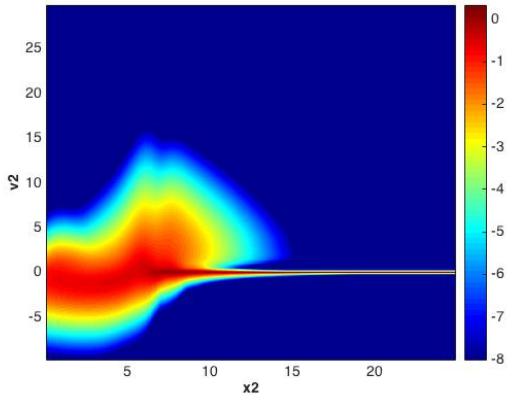

(a) G_h^1, $80 \times 81 \times 82$ mesh

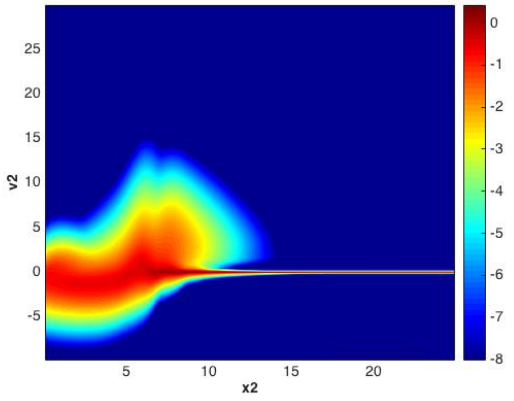

(b) G_h^1, $100 \times 101 \times 102$ mesh

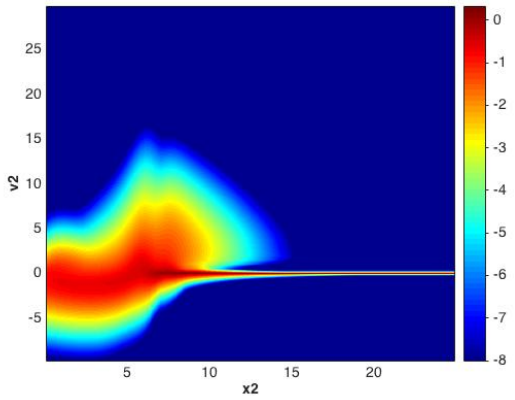

(c) G_h^2, $80 \times 81 \times 82$ mesh

Figure 5.7: Logorithm of the v_1-integrated number density function: $\int f_h dv_1$ in the wakefield acceleration example. Standard DG method with G_h^k, $k = 1, 2$. Positivity-preserving limiter is applied. $T = 10$ and $C_{cfl} = 0.16$.